The Astronomical Journal, 165:258 (19pp), 2023 June https://doi.org/10.3847/1538-3881/acd193

The Emergence of a Neutral Wind Region in the Orbital Plane of Symbiotic Binaries during Their Outbursts

Augustin Skopal
Astronomical Institute, Slovak Academy of Sciences, 059 60 Tatranská Lomnica, Slovakia
Received 2022 November 17; revised 2023 April 17; accepted 2023 April 30; published 2023 May 31

Abstract

Accretion of mass onto a white dwarf (WD) in a binary system can lead to stellar explosions. If a WD accretes from stellar wind of a distant evolved giant in a symbiotic binary, it can undergo occasional outbursts in which it brightens by several magnitudes, produces a low- and high-velocity mass outflow, and, in some cases, ejects bipolar jets. In this paper, we complement the current picture of these outbursts by the transient emergence of a neutral region in the orbital plane of symbiotic binaries consisting of wind from the giant. We prove its presence by determining H^0 column densities (N_H) in the direction of the WD and at any orbital phase of the binary by modeling the continuum depression around the Lyα line caused by Rayleigh scattering on atomic hydrogen for all suitable objects, i.e., eclipsing symbiotic binaries, for which a well-defined ultraviolet spectrum from an outburst is available. The N_H values follow a common course along the orbit with a minimum and maximum of a few times 10^{22} and 10^{24} cm^{-2} around the superior and inferior conjunction of the giant, respectively. Its asymmetry implies an asymmetric density distribution of the wind from the giant in the orbital plane with respect to the binary axis. The neutral wind is observable in the orbital plane owing to the formation of a dense disk-like structure around the WD during outbursts, which blocks ionizing radiation from the central burning WD in the orbital plane.

Unified Astronomy Thesaurus concepts: Symbiotic binary stars (1674); White dwarf stars (1799); Cataclysmic variable stars (203)

1. Introduction

Currently, symbiotic stars (SySts) are understood as the widest interacting binaries comprising a cool giant as the donor and a compact star, mostly a white dwarf (WD), as the accretor. Their orbital periods are typically as long as a few years (S-type systems containing a normal giant; see Belczyński et al. 2000; Gromadzki et al. 2013), but for systems containing a Mira variable (D-type systems; see Webster & Allen 1975; Kenyon et al. 1988; Seal 1990) they can be significantly longer, but mostly they are unknown (e.g., Schmid & Schild 2002; Matthews & Karovska 2006; Hinkle et al. 2013). SySts are detached binaries (Mürset & Schmid 1999); their activity is thus triggered via the wind mass transfer. The accretion process is responsible for the WD's temperatures of (1–2) $\times$ 10^5 K and luminosities of 10^1–10^4 $L_\odot$ (Muerset et al. 1991; Skopal 2005).

According to the light variations in the optical, we distinguish between the quiescent and active phases of SySts. During quiescent phases, an SySt releases its energy at a constant rate. The hot and luminous accreting WD ionizes the neighboring part of the wind from the giant, giving rise to the nebular emission (e.g., Boyarchuk et al. 1966), while its portion around the cool giant remains neutral. The boundary between the ionized and neutral regions is given by the balance between the flux of ionizing photons from the hot component and the flux of neutral particles from the cool giant, the shape of which determines the ionization structure of SySts during the quiescent phase (see, e.g., Figure 6 of Seaquist et al. 1984). This configuration causes the characteristic feature in the light curves of SySts during their quiescent phases—a periodic wave-like variation as a function of the orbital phase (see light curves presented by, e.g., Belyakina 1992; Dmitrienko 2000; Skopal 2008). On the other hand, active phases of SySts result from unstable nuclear burning on the WD surface that gives rise to transient outbursts indicated by brightening of a few magnitudes in the optical. The most characteristic outbursts for SySts are of "Z And type" that result from an increase in the accretion rate above that sustaining the stable burning (Skopal et al. 2017, 2020). They show 1–3 mag (multiple) brightening (s) evolving on the timescale of a few months to years/decades (e.g., Brandi et al. 2005; Leibowitz & Formiggini 2008; Sekeráš et al. 2019) with signatures of a mass outflow (e.g., Fernandez-Castro et al. 1995; Esipov et al. 2000; Skopal 2006; McKeever et al. 2011). The periodic wave-like variation in the light curve disappears, and, in the case of eclipsing systems, deep narrow minima caused by eclipses of the hot component by the red giant appear in the light curve (e.g., Belyakina 1976; see also Appendix B for our targets)—one of the most prominent indications of the change in the ionization structure of the hot component during active phases (see below).

During outbursts, the stellar radiation from the hot component and the nebular radiation markedly change. For systems with a high orbital inclination, the hot component temperature significantly declines, often showing spectral features of an A-to-F-type star in the optical (Mikolajewska & Kenyon 1992, 1996; Munari et al. 1992; Quiroga et al. 2002; Brandi et al. 2005). Such a warm WD pseudophotosphere with an effective radius of several solar radii (Skopal 2005) becomes a significant source of optical radiation. Therefore, its eclipse by the red giant will cause narrow minima in the light curve (see, e.g., Figure 4 of Skopal 2008). Munari et al. (1997a), while studying the active phase of YY Her, pointed out that its hot component cannot always be spherically symmetric, as they indicated its occasionally low temperature ($\sim$1.5 $\times$ 10^4 K) in the simultaneous

presence of a hot subdwarf radiation ($\sim 10^5$ K) in the system. Similarly, during the active phase of AS 338, Esipov et al. (2000) indicated a low hot component temperature ($<1.5 \times 10^4$ K) in the optical with the simultaneous presence of an extended H II region indicating the presence of a high-temperature region ($\sim 10^5$ K) in the "pseudosphere." In this respect, the authors pointed out the similarity with other classical SySts. Another interesting effect, considering the aim of this work, was the appearance of a substantial amount of neutral hydrogen on the line of sight to the hot component of YY Her after its short-duration outburst in 1981 December (Munari et al. 1997). In addition, Quiroga et al. (2002) found that the nebula in AR Pav is probably bounded on all sides by a significant amount of neutral material at least near the orbital plane. In contrast, for noneclipsing systems, seen approximately pole-on, the temperature increases to around 2×10^5 K (e.g., Tomov et al. 2016; Skopal et al. 2020). In both cases, eclipsing and noneclipsing, the nebular continuum increases by a factor of $\sim$10 relative to quiescent phases (Skopal 2005; Skopal et al. 2017). The nature of these dramatic changes between the quiescence and the activity was clarified by disentangling the ultraviolet (UV) to near-infrared spectra of S-type SySts (Skopal 2005). This revealed that all eclipsing systems develop a two-temperature type of the hot component spectrum during active phases: the cool spectrum is produced by a (1–3) $\times 10^4$ K warm pseudophotosphere, while the hot one is represented by highly ionized emission lines and a strong nebular continuum. The former is not capable of producing the measured nebular emission, which thus signals the presence of a strong ionizing source in the system—the essential condition for its interpretation: the hot component has a disk-like structure, whose flared outer rim (which is the warm WD's pseudophotosphere) occults the central ionizing source in the line of sight, while the nebula above/below the disk is ionized (see Figure 27 of Skopal 2005 and Figure 6 of Cariková & Skopal 2012). On the other hand, noneclipsing systems, seen approximately pole-on, show an increase in the WD temperature ($\sim 2 \times 10^5$ K) and the nebular emission from the very beginning of the outbursts (e.g., Skopal et al. 2017).

The key phenomenon, the emergence of the disk-like structure around the WD during active phases, allows us to measure the column density of neutral hydrogen between the observer and the warm WD's pseudophotosphere ($N_{\rm H}^{\rm obs}$) for eclipsing SySts at any orbital phase of the binary (see Figures 8, 10, 19, and 21 of Skopal 2005). This is because the flared disk blocks the ionizing photons from the central hot WD in the orbital plane. Consequently, the lack of ionizing photons allows the giant's wind to remain neutral in the orbital plane.

Accordingly, measuring $N_{\rm H}^{\rm obs}$ from Rayleigh scattering on H atoms around the Lyα line (e.g., Isliker et al. 1989) along the whole orbit, and for all suitable objects (Section 2.1), represents the main aim of this paper. In this way, we revealed the transient emergence of a neutral wind region in the orbital plane and its asymmetry with respect to the binary axis (Section 3). In Section 4 we discuss how our results aid us in understanding the geometric and ionization structure of SySts, while in Section 5 we summarize our findings and propose tasks for future investigation.

2. Observations and Methods

2.1. Selection of Targets

According to the ionization structure of hot components during active phases (see above), the number of objects suitable for the objective of this paper is restricted only to the eclipsing systems, for which a well-defined far-UV spectrum from the active phase is available. This allows us to model the effect of Rayleigh scattering around the Lyα line. Only in such a case is it possible to expect comparable $N_{\rm H}^{\rm obs}$ for different objects at any orbital phase, because their values depend on the orbital inclination. For systems that may no longer be eclipsing but have a relatively high orbital inclination, up to values given by the vertical extension of the WD's pseudophotosphere, lower $N_{\rm H}^{\rm obs}$ values can be expected. For even lower inclinations, when the line of sight passes only through the ionized region, no neutral hydrogen is measurable. Moreover, the wind density dispersion with the orbital inclination can be accentuated by focusing of the giant's wind to the orbital plane (see Shagatova et al. 2016), which results in its dilution around the giant's poles (see Shagatova et al. 2021).

Accordingly, we first inspected the historical light curves of SySts available from the literature, and, on the basis of our own experience with photometric monitoring of these objects for more than 30 yr (Sekeráš et al. 2019), we found that BF Cyg, CH Cyg, CI Cyg, YY Her, BX Mon, AR Pav, AX Per, FN Sgr, PU Vul, AS 338, and AS 296 show eclipses during outbursts. Second, searching the archive of the International Ultraviolet Explorer (IUE), we found that the spectra of Z And, CD $-43°14304$, TX CVn, BF Cyg, CH Cyg, CI Cyg, YY Her, AR Pav, AX Per, PU Vul, AS 338, and AS 296 show signatures of the Rayleigh scattering attenuation around the Lyα line during active phases, which signals a large amount of H atoms on the line of sight. The intersection of both sets of objects should then represent those that best suit the goals of this study. However, some systems from these groups cannot be included in the final set of our targets. They are discussed in Appendix C.

As a result, targets for which comparable $N_{\rm H}^{\rm obs}$ at any orbital phase of the binary can be expected are the eclipsing systems: BF Cyg, CI Cyg, YY Her, AR Pav, AX Per, and PU Vul. The log of their IUE spectra is introduced in Table 1, and Appendix D summarizes their basic characteristics.

2.2. Measuring $N_{\rm H}^{\rm obs}$ from Rayleigh Scattering

Rayleigh scattering represents the process where the atom is excited by an incident photon to the intermediate state and is immediately stabilized by a transition to the same bound state, reemitting a photon of the original energy (e.g., Nussbaumer et al. 1989). For hydrogen, the effect is best observable around the Lyα line as a continuum depression with zero residual intensity and extended wings. The strength of Rayleigh scattering is determined by the number of scatterers on the path between the emitting source and the observer, i.e., on the value of $N_{\rm H}^{\rm obs}$, and its profile is given by the cross section, $\sigma_{\rm Ray}(\lambda)$, which yields the optical depth, $\tau_{\rm Ray} = \sigma_{\rm Ray}(\lambda) N_{\rm H}^{\rm obs}$. Therefore, fitting the far-UV continuum of an object attenuated by Rayleigh scattering, we can obtain the corresponding value of $N_{\rm H}^{\rm obs}$. It is important to emphasize that the Rayleigh scattering effect is dominant in modeling the continuum depression around the Lyα line[1] during quiescent phases (e.g., Isliker et al. 1989; Vogel 1991; Dumm et al. 1999;

[1] It is meant relative to other line-broadening effects in the neutral part of the giant's wind.

Table 1
Log of the Low-resolution IUE Spectra of Our Targets and Corresponding Column Densities $N_{\rm H}^{\rm obs}$ (see Text and Figure 1)

Object	Spectrum	Date (UT)[a] (yyyy-mm-dd)	Julian Date[a] (JD 2 44...)	φ[b]	$N_{\rm H}^{\rm obs}$ ($\rm cm^{-2}$)
BF Cyg[c]	SWP31540+LWP11376	1987-08-11	7019.35	0.145	$(2.5 \pm 1.0) \times 10^{23}$
	SWP32341+LWP12109	1987-11-16	7116.00	0.273	$(9.0\ +2.4/-1.9)\times10^{22}$
	SWP33113+LWP12886	1988-03-19	7239.88	0.436	$(3.5 \pm 1.1) \times 10^{22}$
	SWP39163+LWP18251	1990-06-30	8072.58	0.536	$(4.8 \pm 1.5) \times 10^{22}$
	SWP39188+LWP18302	1990-07-06	8079.35	0.545	$(6.0 \pm 1.8) \times 10^{22}$
	SWP40055+LWP19153(4)	1990-11-05	8201.25	0.706	$(4.0\ +1.2/-1.5)\times10^{22}$
CI Cyg[d]	SWP03816+LWR03396	1979-01-05	3879.35	0.392	$(7.0 \pm 2.7) \times 10^{22}$
	SWP05485+LWR04757	1979-06-11	4035.74	0.576	$(3.0 \pm 1.3) \times 10^{22}$
	SWP05672+LWR04916	1979-06-29	4054.03	0.597	$(3.5 \pm 1.4) \times 10^{22}$
	SWP07818+LWR06831	1980-01-30	4269.40	0.850	$(1.6 \pm 0.7) \times 10^{23}$
	SWP08757	1980-04-14	4344.17	0.937	$(2.5\ +0.9/-0.8)\times10^{24}$
	SWP09664+LWR08408	1980-08-01	4453.21	0.065	$(1.5 \pm 0.7) \times 10^{24}$
	SWP09830+LWR08542	1980-08-18	4469.96	0.085	$(1.0\ +0.6/-0.4)\times10^{24}$
	SWP09942+LWR08651	1980-08-28	4480.44	0.097	$(6.0\ +1.6/-2.6)\times10^{23}$
	SWP10602+LWR09303	1980-11-14	4558.37	0.188	$(2.5 \pm 0.8) \times 10^{23}$
	SWP11003+LWR09671	1981-01-08	4613.44	0.253	$(1.0\ +0.5/-0.3)\times10^{23}$
	SWP14755+LWR11318	1981-08-14	4830.93	0.508	$(6.0 \pm 2.6) \times 10^{22}$
	SWP15713+LWR12127	1981-12-11	4950.19	0.648	$(3.0 \pm 1.3) \times 10^{22}$
YY Her[e]	SWP15652+LWR12080	1981-12-04	4943.46	0.265	$(1.4\ +0.4/-0.6)\times10^{23}$
AR Pav[f]	SWP17070+LWR13346	1982-05-30	5119.91	0.008	eclipse
	SWP10415+LWR09095	1980-10-19	4532.05	0.035	eclipse
	SWP10497+LWR09184	1980-10-29	4541.85	0.051	eclipse
	SWP10510+LWR09199	1980-10-30	4543.45	0.054	$(3.0 \pm 1.3) \times 10^{24}$
	SWP10520+LWR09207	1980-11-01	4544.90	0.056	$(3.0 \pm 1.3) \times 10^{24}$
	SWP10524+LWR09212	1980-11-02	4545.74	0.058	$(2.5 \pm 1.3) \times 10^{24}$
	SWP10527+LWR09217	1980-11-03	4546.70	0.059	$(2.5 \pm 1.3) \times 10^{24}$
	SWP17331+LWR13580	1982-07-01	5152.09	0.061	$(2.5\ +0.8/-1.3)\times10^{24}$
	SWP22434+LWP02903	1984-03-07	5766.70	0.078	$(2.0 \pm 0.7) \times 10^{24}$
	SWP45099+LWP23467	1992-07-08	8812.01	0.116	$(5.0\ +1.5/-2.5)\times10^{23}$
	SWP22707+LWP03139	1984-04-10	5800.76	0.134	$(4.0 \pm 1.4) \times 10^{23}$
	SWP05828+LWR05077	1979-07-17	4071.74	0.274	$(7.5\ +1.8/-3.3)\times10^{22}$
	SWP13956+LWR10570	1981-05-10	4735.37	0.371	$(5.0 \pm 2.0) \times 10^{22}$
	SWP01561	1978-05-16	3645.37	0.568	$(5.0\ +3.5/-2.5)\times10^{22}$
	SWP02236+LWR02023	1978-08-08	3728.89	0.706	$(3.0 \pm 1.3) \times 10^{22}$
	SWP03310+LWR02917	1978-11-11	3824.39	0.864	$(2.0\ +1.7/-0.7)\times10^{23}$
	SWP09646+LWR08393	1980-07-30	4451.29	0.901	$(1.9\ +0.7/-0.8)\times10^{24}$
	SWP16711+LWR12974	1982-04-07	5067.04	0.920	$(1.0\ +0.6/-0.4)\times10^{24}$
	SWP16857+LWR13104	1982-04-29	5088.99	0.956	eclipse
	SWP16938+LWR13208	1982-05-09	5098.88	0.973	eclipse
	SWP16949+LWR13235	1982-05-13	5102.93	0.980	eclipse
AX Per[g]	SWP03755+LWR03332	1978-12-31	3873.65	0.598	$(5.0\ +2.5/-1.5)\times10^{22}$
	SWP03814+LWR03332	1979-01-05	3879.19	0.606	$(4.5\ +2.5/-1.5)\times10^{22}$
PU Vul[h]	SWP33833+LWP13531	1988-06-29	7342.30	0.570	$(5.6 \pm 1.8) \times 10^{22}$
	SWP33930+LWP13669	1988-07-16	7359.45	0.574	$(5.8 \pm 1.9) \times 10^{22}$
	SWP34406+LWP14173	1988-10-03	7437.82	0.590	$(3.9 \pm 1.5) \times 10^{22}$
	SWP35960+LWP15328	1989-04-08	7624.82	0.628	$(3.0 \pm 0.9) \times 10^{22}$
	SWP36301+LWP15549	1989-05-19	7666.20	0.636	$(2.9 \pm 1.2) \times 10^{22}$
	SWP37185+LWP16416	1989-09-25	7794.53	0.663	$(3.8 \pm 1.4) \times 10^{22}$
AS 338[i]	SWP37290+LWP16522	1989-10-09	7809.16	0.670	$<5 \times 10^{23}$
AS 296[j]	SWP34080+LWP13843	1988-08-13	7387.15	0.321	$(1.0\ +2.1/-0.6)\times10^{23}$
	SWP34725+LWP14446	1988-11-11	7477.07	0.458	$<3 \times 10^{23}$
	SWP38353+LWP17523	1990-03-13	7963.90	0.197	$(3.0 \pm 2.3) \times 10^{23}$

Notes.
[a] The dates correspond to the start of the observation with the SWP camera.
[b] Orbital phase as given by the ephemerides below.
[c] $\rm JD_{spec.conj.} = 2{,}445{,}395.1 + 757.2 \times E$ (Fekel et al. 2001), $E_{B-V} = 0.35$, $d = 3.4$ kpc (Muerset et al. 1991).
[d] $\rm JD_{ecl.} = 2{,}441{,}838.8 + 852.98 \times E$ (Skopal et al. 2012), $E_{B-V} = 0.35$ (Skopal 2005), $d = 1.6$ kpc (Seaquist et al. 1993).
[e] $\rm JD_{ecl.} = 2{,}440{,}637 + 592.8 \times E$ (Skopal 1998), $d = 6.3$ kpc (Skopal 2005), $E_{B-V} = 0.20$ (Munari et al. 1997).
[f] $\rm JD_{ecl.} = 2{,}411{,}266.1 + 604.45 \times E$ (Skopal 2005), $E_{B-V} = 0.26$, $d = 4.9$ kpc (Schild et al. 2001).
[g] $\rm JD_{ecl.} = 2{,}447{,}551.26 + 680.83 \times E$ (Skopal et al. 2011), $E_{B-V} = 0.27$ (Kenyon & Webbink 1984), $d = 1.7$ kpc (Skopal et al. 2001).
[h] $\rm JD_{ecl.} = 2{,}444{,}550 + 4897 \times E$ (Shugarov et al. 2012), $E_{B-V} = 0.30$, $d = 4.7$ kpc (Kato et al. 2012).
[i] $\rm JD_{ecl.} = 2{,}446{,}650 + 434.1 \times E$ (Siviero et al. 2007), $E_{B-V} = 0.50$, $d = 6$ kpc (Esipov et al. 2000).
[j] $\rm JD_{ecl.} = 2{,}448{,}492 + 658 \times E$ (Munari et al. 1995), $E_{B-V} = 1.0$, $d = 1$ kpc (Munari et al. 1992).

Crowley et al. 2005) and also in our case, during active phases, because the width of the possible "atmospheric" Lyα absorption profile from/above the warm WD pseudophotosphere can be neglected (see Appendix F).

According to the configuration of SySts, we assume that the UV continuum of eclipsing systems during outbursts consists of the stellar continuum from the warm WD's pseudophotosphere and the nebular continuum from the ionized circumbinary matter (see Section 1). We compare the former with the blackbody radiation at a temperature $T_{\rm BB}$ and approximate the latter by contributions from free–bound and free–free transitions in hydrogen plasma radiating at the electron temperature T_e. Then, using Equations (5) and (11) of Skopal (2005), the reddening-free UV continuum of an SySt, $F(\lambda)$, measured at Earth, can be written in the form

$$F(\lambda) = \theta_{\rm WD}^2 \pi B_\lambda(T_{\rm BB}) e^{-\sigma_{\rm Ray}(\lambda) N_{\rm H}^{\rm obs}} + k_{\rm N} \times \varepsilon_\lambda({\rm H}, T_e), \quad (1)$$

where $\theta_{\rm WD} = R_{\rm WD}^{\rm eff}/d$ is the angular radius of the warm WD's pseudophotosphere, given by its effective radius $R_{\rm WD}^{\rm eff}$ (i.e., the radius of a sphere with the same luminosity) and the distance d. The Rayleigh cross section for scattering by hydrogen in its ground state can be expressed as (see Nussbaumer et al. 1989)

$$\sigma_{\rm Ray}(\lambda) = \sigma_e \left[\sum_k \frac{f_{1k}}{(\lambda/\lambda_{1k})^2 - 1} \right]^2, \quad (2)$$

where $\sigma_e = 6.65 \times 10^{-25}$ cm^2 is the Thomson cross section, f_{1k} are the oscillator strengths of the hydrogen Lyman series, and λ_{1k} are the corresponding wavelengths. In calculating $\sigma_{\rm Ray}(\lambda)$, we used all bound states tabulated by Wiese et al. (1966), i.e., $k = 2$–40. The second term on the right-hand side is the nebular continuum given by its volume emission coefficient, $\varepsilon_\lambda({\rm H}, T_e)$, scaled with the factor $k_{\rm N} = {\rm EM}/4\pi d^2$, where EM is the emission measure of the nebula. The variables determining the model continuum are $\theta_{\rm WD}$, $T_{\rm BB}$, $N_{\rm H}^{\rm obs}$, $k_{\rm N}$, and T_e. They are obtained by comparing Equation (1) with the continuum fluxes selected from the dereddened spectra of our targets. In selecting suitable flux points of the true continuum, we proceeded as follows.

First, we considered the influence of the line-blanketing effect, which represents an additional source of absorption in the neutral wind, mostly by Fe II transitions (see Shore & Aufdenberg 1993). This so-called iron curtain can strongly depress the level of the continuum at 1500–1800 Å and 2300–2800 Å (see, e.g., BF Cyg, PU Vul, and AR Pav in Appendices A and B). To eliminate this effect, we used a template of three representative low-resolution IUE spectra with a low, modest, and strong influence of the continuum by the iron curtain (see Figure 1 of Skopal 2005). With the aid of these observations and theoretical calculations of, e.g., Shore & Aufdenberg (1993) and Horne et al. (1994), we selected spectral regions with the lowest effect of the intervening absorption. Second, we took into account the often very different errors of the measured fluxes for different spectra, which are also wavelength dependent. For example, in the short-wavelength part of the spectrum, especially below 1200 Å, the standard deviation of the flux measurement can be compared to the flux itself.[2] Fortunately, the use of only the fluxes of the long-wavelength wing of the Rayleigh-attenuated continuum is sufficient to determine the values of $N_{\rm H}^{\rm obs}$ (e.g., Vogel 1991; Fernandez-Castro et al. 1995). Furthermore, the very extended absorption profile for $N_{\rm H}^{\rm obs} \gtrsim 2 \times 10^{22}$ cm^{-2} causes a measurable Rayleigh scattering effect even for $\lambda > 1300$ Å (see Figure 5 in Appendix F), where the spectrum is in most cases sufficiently well determined to allow us to at least estimate the corresponding value of the H^0 column density. However, for some strongly underexposed spectra, it was possible to estimate only the upper limit of $N_{\rm H}^{\rm obs}$ or its wide range. Therefore, according to the quality of the used spectra, we proceeded to determine the $N_{\rm H}^{\rm obs}$ values as follows:

(i) For well-exposed spectra, according to the signal-to-noise ratio and for simplicity, we set the errors to 7%–10% for all selected continuum fluxes. In these cases, we calculated a grid of models (1) for reasonable ranges of the fitting parameters and selected that corresponding to a minimum of the reduced χ^2 function.[3]

(ii) In cases where the spectrum is underexposed, mostly in the far-UV region and/or regions heavily affected by the iron curtain absorptions, we compared the spectrum to a set of plausible synthetic models, $(\lambda, B_\lambda(T_{\rm BB})\exp[-\sigma_{\rm Ray}(\lambda)N_{\rm H}^{\rm obs}], \varepsilon_\lambda({\rm H}, T_e)$, and selected the best match by eye.

(iii) Finally, for severely underexposed spectra of AS 338 and AS 296, we estimated only the upper limits or wide ranges of H^0 column densities (see Appendix C and examples in the bottom row of Figure 3). Some example models for our targets are shown in Figure 3 (Appendix A). Examples of the selected continuum fluxes for better-exposed (PU Vul) and poorly exposed (AR Pav) far-UV spectra with the corresponding models are illustrated in Figure 7 (Appendix G).

The most important parameter for the purpose of this paper is the column density $N_{\rm H}^{\rm obs}$ (Table 1), in particular, its dependence on the orbital phase (Figure 1). Its uncertainty is estimated at ~20%–60%, depending on the signal-to-noise ratio and the influence of other emission features around the Lyα transition. For illustration, the models corresponding to the upper and lower values of $N_{\rm H}^{\rm obs}$ are depicted by dotted lines in Figures 3 and 4. In addition, we also investigated the possible dependence of the $N_{\rm H}^{\rm obs}$ determination on interstellar reddening. Our analysis suggests that uncertainties in the E_{B-V} color excess may cause additional errors in the $N_{\rm H}^{\rm obs}$ determination of about 10% (see Appendix G). Table 1 and Figure 1 indicate the total $N_{\rm H}^{\rm obs}$ errors. For completeness, Table 3 (Appendix E) presents the values of other parameters determining the UV continuum. Their uncertainties would be estimated at ~10%–50% of their best values (see Section 3.3 of Skopal 2005).

3. Results

3.1. Indication of the Neutral Wind Region in the Orbital Plane during Outbursts

The main result of this study is depicted in Figure 1: the $N_{\rm H}^{\rm obs}$ values for our targets show a strong dependence on the orbital phase, with a difference of about two orders of magnitude between the values around the inferior and superior conjunction of the giant. High values of $N_{\rm H}^{\rm obs}$ at any position of the binary reflect the presence of a neutral region in the orbital plane, because our targets are seen approximately edge-on. Its

[2] However, there are spectra that are quite well exposed even below 1200 Å. In these cases the model matches also the short-wavelength wing of the continuum depression (e.g., PU Vul and BF Cyg; see Appendix A).

[3] The corresponding software and application example are available at Zenodo Skopal (2023).

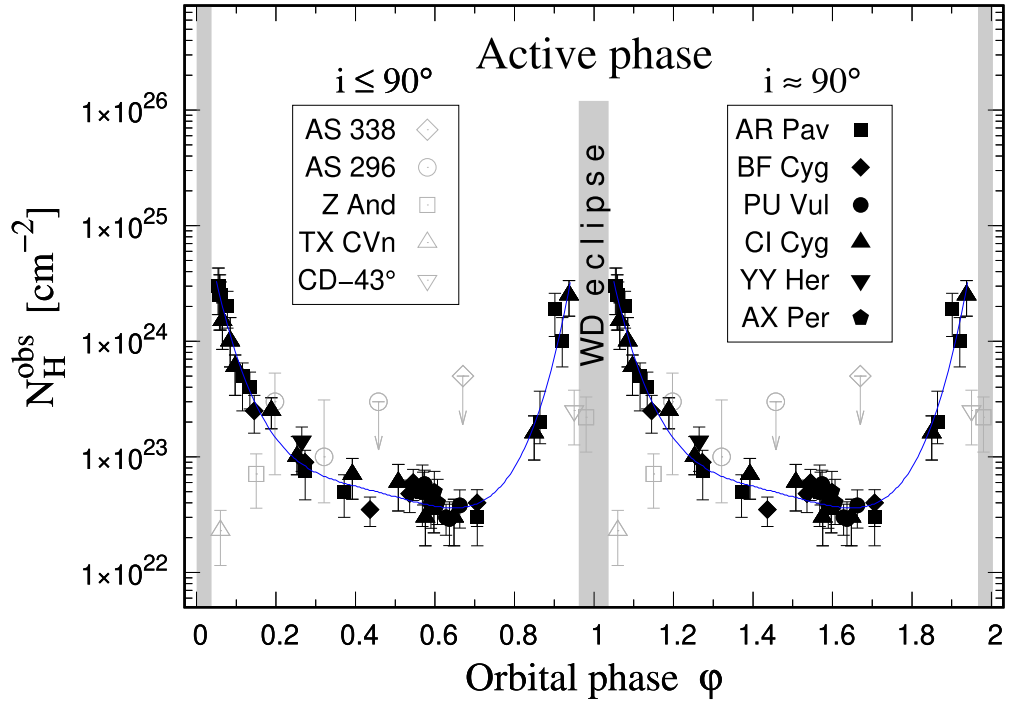

Figure 1. Column densities of atomic hydrogen, N_H^{obs}, between the observer and the WD, measured for our targets (Section 2.1) during active phases as a function of the orbital phase φ ($\varphi = 0$ corresponds to the inferior conjunction of the giant). For better visualization, the values are plotted over two orbital cycles. Eclipsing objects (black filled symbols) follow a common course. The blue line indicates their fit with a fourth-degree polynomial. Open gray symbols denote values for objects discussed in Appendix C, i.e., for those with poorly defined UV spectra (AS 338, AS 296) or not eclipsing, but with a high orbital inclination (Z And, TX CVn, CD −43°14304 (CD−43° in the legend)). Values for the latter were taken from Skopal (2005). All data measured in this work are summarized in Table 1, and examples of the corresponding continuum models are shown in Appendix A.

emergence is transient, being connected solely with active phases (Section 3.2, Appendix B). The values for eclipsing systems (i.e., BF Cyg, CI Cyg, YY Her, AR Pav, AX Per, and PU Vul) follow a common course that suggests similar properties of the neutral zone for these objects. In contrast, during quiescent phases of eclipsing systems, the neutral hydrogen zone is limited only to the vicinity of the inferior conjunction of the giant, where it represents the neutral wind from the giant (e.g., Vogel 1991; Dumm et al. 1999; Shagatova & Skopal 2017). Therefore, a comparison of H^0 column densities from quiescent and active phases at these positions (see Figure 2, panels (b) and (e)) suggests that our N_H^{obs} values also represent the densities of the stellar wind from the giant.

The case of measuring the H^0 column densities in the direction to the WD, while the source of neutral hydrogen is associated with the red giant, will give a large difference between their values measured around the inferior and the superior conjunction of the giant, which is in agreement with our result (see Figure 1). Thus, the high-amplitude orbital-dependent variation of N_H^{obs} values confirms that we measure H^0 column densities of the neutral wind from the red giant.[4]

3.2. The Cause of the Neutral Region during Outbursts

The emergence of the neutral wind region in the orbital plane is conditioned by the formation of an optically thick disk-like structure around the WD in the orbital plane during outbursts (see Section 1). Consequently, the disk blocks the ionizing radiation from the central burning WD within its vertical extension from the orbital plane, which makes the wind of the giant neutral in the orbital plane, thus making it detectable by eclipsing systems in any orbital phase. During active phases, the wind from the giant represents a cool absorbing gas veiling the WD's pseudophotosphere in the orbital plane. Therefore, the N_H^{obs} values of this medium show a clear dependence on the orbital phase, with a high amplitude (Figure 1, Section 3.1).

The presence of the neutral giant's wind in the orbital plane is primarily indicated by the deep continuum depression in the spectrum around the Lyα line due to Rayleigh scattering on H^0 atoms and by broad absorption bands due to the iron curtain (see Figure 3),[5] the features that are absent during quiescent phases around the whole orbit. For our targets, we demonstrate the corresponding change of the UV spectrum between the quiescent and active phases in Figure 4 (Appendix B).

3.3. Wind Asymmetry

Figure 1 shows the asymmetric distribution of N_H^{obs} values along the orbit with a minimum of $\sim 4 \times 10^{22}$ cm^{-2} between $\varphi \sim 0.6$ and ~ 0.7 and a maximum of a few times 10^{24} cm^{-2} just before and after eclipses ($\varphi \sim 0.95$ and ~ 0.03). The asymmetry is also evidenced by the steeper values of N_H^{obs} before the eclipse ($0.85 < \varphi < 0.95$) than after the eclipse ($\varphi > 0.05$) and a small local maximum around $\varphi = 0.5$. Such asymmetric distribution of N_H^{obs} along the orbit implies the asymmetric density distribution of the giant's wind in the near-orbital-plane region with respect to the binary axis. This property of the wind was previously indicated also for quiescent eclipsing SySts SY Mus and EG And by the same type of asymmetric distribution of H^0 column densities,

[4] If the broad Lyα line profile was formed in the WD atmosphere, there would be no reason to measure the dependence of the N_H^{obs} values on the orbital phase (see the last paragraph of Appendix F).

[5] The prominence of the iron curtain in the spectrum varies from object to object, depending mainly on the temperature of the WD's pseudophotosphere.

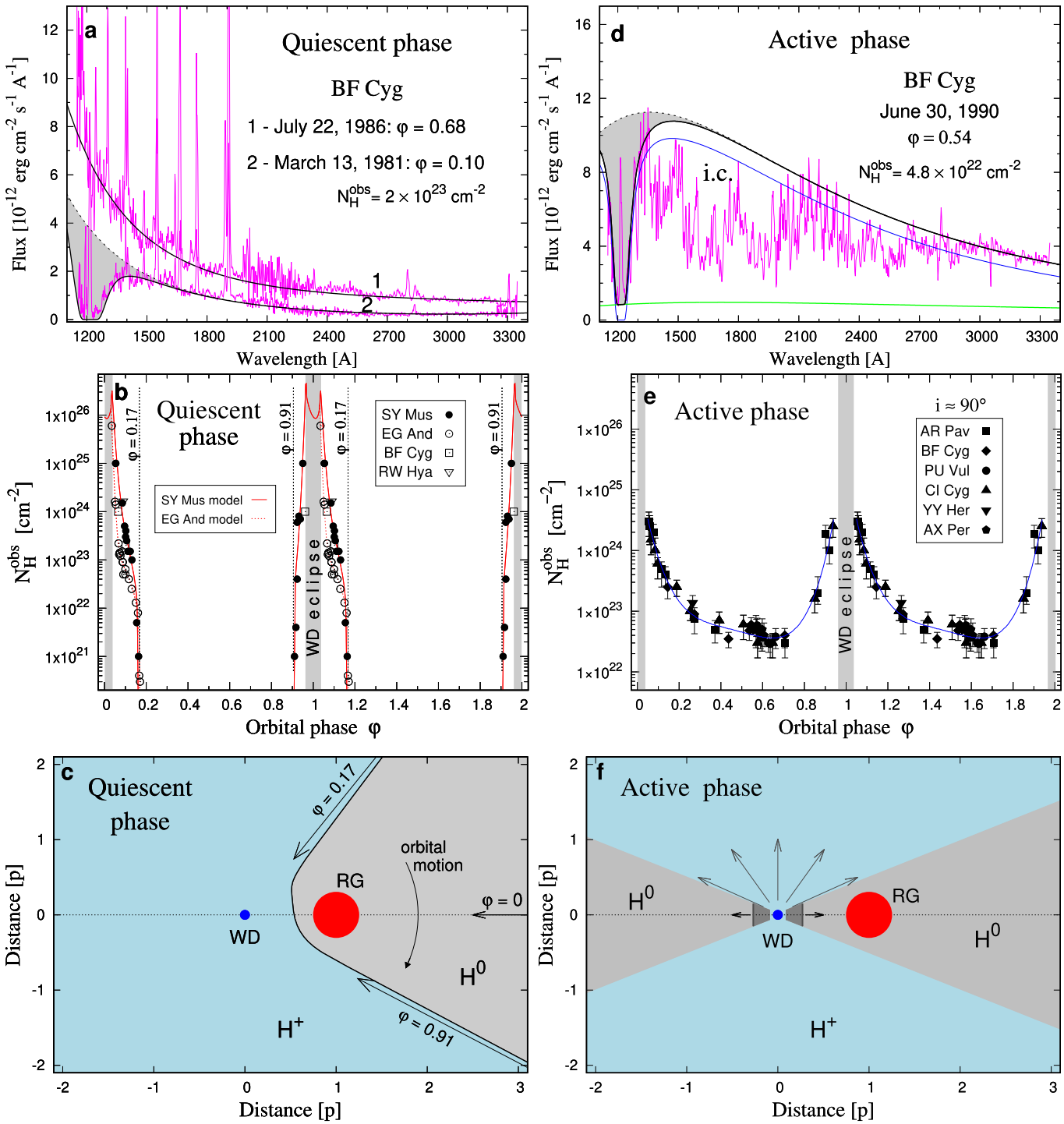

Figure 2. The symbiotic phenomenon in a nutshell. Characteristic UV spectra (top panels), hydrogen column densities $N_{\rm H}^{\rm obs}$ (middle panels), and sketch of the corresponding ionization structure (bottom panels) for eclipsing SySts (see keys) during quiescent and active phases are shown in the left and right columns, respectively. During the quiescent phase, the ionization structure is given by the location of $N_{\rm H}^{\rm obs}$ values only in the vicinity of the inferior conjunction of the giant (pole-on view; see Shagatova & Skopal 2017), while during the active phase a biconical ionization structure is constrained by the H^0 wind region in the orbital plane (edge-on view; Section 4.2). The two-velocity type of mass outflow during outbursts is denoted by arrows of different sizes (Section 4.2). In both cases, the asymmetric profile of $N_{\rm H}^{\rm obs}(\varphi)$ (panels (b) and (e)) imprints the asymmetric wind from the giant. Spectra from the quiescent phase (panel (a)) are introduced in Table 4 (Appendix E). Description of SED models is as in Appendix A, and column densities in panel (e) are as in Figure 1. The data and models in panel (b) are from the literature (see Section 4.1), i.c. denotes the continuum depression caused by the iron curtain (see Section 2.2), and p is in units of the binary components' separation. Other denotations are obvious.

although they are measurable only around the inferior conjunction of their giants in quiescent phases (Dumm et al. 1999; Shagatova et al. 2016; here Figure 2(b), Section 4.1). Recently, this sort of asymmetric shaping of the wind in the orbital plane was confirmed by modeling the UV light curves of SY Mus (Shagatova & Skopal 2017) and by the Hα line profile variation along the orbit of EG And (Shagatova et al. 2021). Therefore, the orbital-dependent asymmetry of $N_{\rm H}^{\rm obs}$ values measured for more

objects and during the active phases (Figure 1) suggests that the asymmetric distribution of the giant's wind in the orbital plane with respect to the binary axis may possibly be a common property of winds from giants in SySts.

Its origin could in principle be similar to that simulated and measured for detached high-mass X-ray binaries consisting of a hot O/B (super)giant and a neutron star or a black hole, where a similar type of orbital-related asymmetry in $N_{\rm H}$ is attributed to tidal streams and accretion wakes, distorted by the orbital motion (e.g., Blondin et al. 1990, 1991; Manousakis et al. 2012; Kretschmar et al. 2021; Rahin & Behar 2023). Modeling of our $N_{\rm H}^{\rm obs}(\varphi)$ values in this way, but for parameters of S-type SySts, should clarify the cause of their asymmetric distribution throughout the orbit.

4. Discussion

Here we describe how our findings complement the overall picture of the symbiotic phenomenon. For this purpose, we present the characteristic UV spectra of SySts and the measured H^0 column densities as a function of the orbital phase, and we discuss how they relate to the ionization structure of SySts during both the quiescent and active phases. Figure 2 summarizes our view.

4.1. Quiescent Phase

During quiescent phases, the far-UV spectrum is dominated by the Rayleigh–Jeans tail of a very hot source of the stellar radiation ($T_{\rm BB} \gtrsim 10^5$ K), while the near-UV is usually dominated by the nebular continuum (e.g., Muerset et al. 1991; Skopal 2005). The effect of Rayleigh scattering on hydrogen atoms and the overall decrease of the continuum level are measured only for eclipsing systems in the vicinity of the inferior conjunction of the giant as a result of the passage of light from the WD through the absorbing medium of the neutral wind from the giant (e.g., Isliker et al. 1989; Horne et al. 1994). Here an example of BF Cyg is depicted in Figure 2(a). Figure 2(b) then shows all $N_{\rm H}^{\rm obs}$ values of eclipsing SySts determined during their quiescent phases: SY Mus and EG And (Dumm et al. 1999; Shagatova et al. 2016), BF Cyg (Pereira & Landaberry 1996), and RW Hya (Dumm et al. 1999). Accordingly, the observed distribution of H^0 column densities along the orbit suggests that the neutral zone is located around the giant and beyond it in the direction away from the WD, and it is distributed asymmetrically with respect to the binary axis, while the rest of the binary environment around the WD is ionized. An example of SY Mus that corresponds to the $N_{\rm H}^{\rm obs}(\varphi)$ model depicted in Figure 2(b) (red line; Shagatova et al. 2016) is shown in Figure 2(c) (adapted according to Shagatova & Skopal 2017). A simplified calculation of the ionization H^0/H^+ boundary during the quiescent phase is introduced by Seaquist et al. (1984) and Nussbaumer & Vogel (1987).

4.2. Active Phase

During active phases, the UV spectrum of eclipsing SySts can be fitted by a low-temperature stellar type of radiation ($T_{\rm BB} \approx (1\text{–}3) \times 10^4$ K) emitted by the warm WD's pseudophotosphere often dominating the far-UV and a strong nebular continuum pronounced in the near-UV (see examples in Appendices A and B). The former is strongly attenuated around the Lyα line by Rayleigh scattering on H^0 atoms at any orbital phase and shows signatures of the iron curtain absorptions, while the latter increases compared to the quiescent phase (Figure 2(d), and Appendices A and B). The corresponding high values of $N_{\rm H}^{\rm obs}$ along the orbit (Figure 1) indicate the presence of the neutral region in the orbital plane (Section 3).[6] Such a neutral zone determines a biconical shaping of the ionized region distributed above/below it, with the tops at the burning WD (see Figure 2(f)). In this case, the nebular radiation is produced by the ionized wind from the WD (Skopal 2006). Such an ionization structure is responsible for observing two different types of spectra depending on the orbital inclination. This suggests a classification of outbursts into two types: the warm type and hot type (see also Skopal 2005; Skopal et al. 2020).

(i) Outbursts in systems with a high orbital inclination (i.e., seen approximately edge-on) show the two-temperature type of the hot component spectrum (see Section 1). These outbursts are classified as the "warm type" because the stellar component of radiation is emitted by the warm ($(1\text{–}3) \times 10^4$ K) WD's pseudophotosphere. During the warm type of outbursts, the two-velocity type of mass outflow from the hot component is indicated. A rather slow outflow is indicated by the absorption component in P Cygni line profiles created in the expanding optically thick wind from the WD in the orbital plane, while a fast outflow is indicated by the broad emission wings produced by the fast optically thin ionized wind from the WD over the remainder of the star (see Figure 2(f), and Skopal et al. 2006, in detail). All our targets show signatures of the warm-type of outbursts.

(ii) Outbursts in systems with a low orbital inclination (i.e., seen approximately pole-on) show the spectrum characterized by the immediate occurrence of strong nebular radiation that dominates the optical. These outbursts are classified as "hot type" because the stellar component of radiation is emitted by the hot ($\sim 2 \times 10^5$ K) WD's pseudophotosphere, the contribution of which is negligible in the optical (e.g., Skopal et al. 2020). The strong nebular radiation is emitted by the enhanced ionized wind from the WD (Skopal 2006). Here the well-observed SySts AG Dra, AG Peg, LT Del, and V426 Sge show features of the hot type of outbursts (e.g., González-Riestra et al. 2008; Leedjärv et al. 2016; Skopal et al. 2017; Ikonnikova et al. 2019; Skopal et al. 2020).

5. Conclusion and Future Work

We have found that a deep and wide absorption is formed around the Lyα line during outbursts of all eclipsing symbiotic binaries around the whole orbit, for which there are relevant observations (Section 2.1). Modeling this feature by Rayleigh scattering on atomic hydrogen, we determined the corresponding H^0 column densities in the direction of the WD (Figure 1). The high values of $N_{\rm H}^{\rm obs}$ measured at any orbital phase indicate the presence of a neutral region in the orbital plane. Their large-amplitude orbital-dependent variation indicates that this region consists of the wind from the giant (Section 3.1). It is observable owing to the emergence of a dense disk-like structure around the WD during outbursts (Skopal 2005; Cariková & Skopal 2012) that blocks the ionizing photons from the central hot WD in the orbital plane (Section 3.2). The asymmetric course of $N_{\rm H}^{\rm obs}(\varphi)$ values implies

[6] During outbursts of noneclipsing systems, the neutral wind region in the orbital plane is indicated by significant broadening and high fluxes of the Raman-scattered O VI 6825 Å line relative to the quiescent phase. This is because the new neutral hydrogen in the orbital plane increases the Raman scattering efficiency (see Skopal et al. 2020).

an asymmetric density distribution of the wind from the giant in the orbital plane with respect to the binary axis (Section 3.3). Finally, the emergence of the neutral near-orbital-plane region changes significantly the ionization structure of the symbiotic binary during active phases: the ionized region is distributed above/below it, having the tops at the burning WD (Section 4.2, Figure 2(f)).

The unique distribution of neutral hydrogen in the orbital plane of symbiotic binaries as indicated for different objects during different stages of their activity (Figure 1, Appendix B) suggests common properties of stellar winds from their giants. Our findings can aid us in further theoretical modeling and can be conducive to the explanation of more violent classical nova outbursts. For example:

1. Modeling $N_{\rm H}^{\rm obs}$ values along the whole orbit for more objects during active phases should confirm and generalize the substantial focusing of the wind from the giant in S-type SySts toward the orbital plane as found for quiescent SySts SY Mus and EG And by Shagatova et al. (2016, 2021).
2. The $N_{\rm H}^{\rm obs}$ values measured around the orbit will serve as a benchmark for testing the theoretical modeling of the wind morphology of wide interacting binaries containing an evolved giant (e.g., Bermúdez-Bustamante et al. 2020; El Mellah et al. 2020; Lee et al. 2022). In particular, modeling the morphology of a massive slow wind blowing from red giants in S-type SySts with terminal velocity of a few times $10\,{\rm km\,s^{-1}}$ (e.g., Dumm et al. 1999), at rates of a few times $(10^{-7}$–$10^{-6})\,M_{\odot}\,{\rm yr^{-1}}$ (e.g., Seaquist et al. 1993; Shagatova et al. 2016), which is disrupted by the accreting WD, in a similar way to what has been done for massive X-ray binaries (see references in Section 3.3), should lead to a better understanding of the mass transfer problem in symbiotic binaries.
3. The emergence of a slowly expanding disk-like structure around the exploding WD appears to be common also for more violent outbursts of classical novae, where it is indicated by direct radio imaging (Chomiuk et al. 2014) and is constrained by modeling the energy distribution in the nova spectrum (Skopal 2019). During outbursts of SySts, the flared disk blocks the ionizing radiation from the center, resulting in the creation of the neutral near-orbital-plane region throughout the binary. During the classical nova explosions, the disk represents a vital element to explain the γ-ray emission measured near the optical maximum as a result of shocks developing between the first slow and secondary fast outflow (e.g., Li et al. 2017). In addition, the disk structure facilitates the creation of dust and its persistence during extreme conditions of the supersoft X-ray phase (e.g., Skopal 2019).

I thank my colleague Ján Budaj for having calculated for me the Lyα profiles discussed in Appendix F. This work was supported by a grant of the Slovak Academy of Sciences, VEGA No. 2/0030/21, and by the Slovak Research and Development Agency under contract No. APVV-20-0148. This research is based on observations made with the International Ultraviolet Explorer, obtained from the MAST data archive at the Space Telescope Science Institute, which is operated by the Association of Universities for Research in Astronomy, Inc., under NASA contract NAS 5-26555.

Facilities: IUE(SWP, LWP), AAVSO.

The data presented in this paper were obtained from the Mikulski Archive for Space Telescopes (MAST) at the Space Telescope Science Institute. The specific IUE observations analyzed can be accessed via DOI:10.17909/0mkj-f579.

Appendix A
Indication of Neutral Hydrogen in the Orbital Plane of Eclipsing Symbiotic Stars during Their Active Phases

Figure 3 shows examples of spectral energy distribution (SED) models in the UV for the investigated objects at different orbital phases (see Section 2.2).

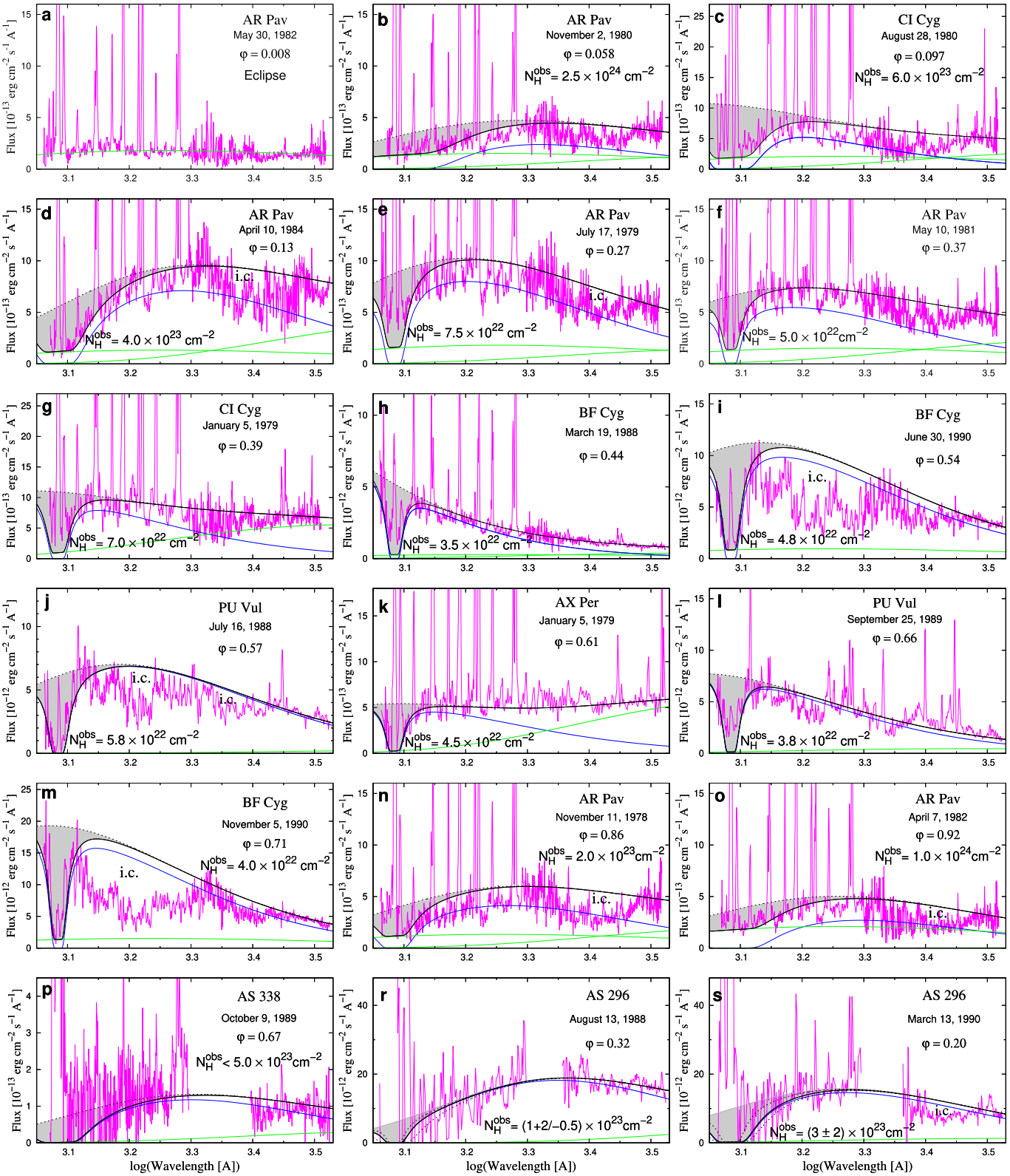

Figure 3. Examples of IUE spectra (in magenta) of our targets (Section 2.1) during active phases observed at different orbital phases φ and their SED model (black line, Equation (1)). The model consists of the nebular (green lines) and the stellar continuum from the hot component (blue line; Section 2.2). A strong depression of the continuum around the Lyα line (gray area) is caused by Rayleigh scattering of the WD radiation on hydrogen atoms with column densities, $N_{\rm H}^{\rm obs}$ (Table 1). The bottom row shows examples of AS 338 and AS 296, whose spectra are underexposed (see Appendix C). Models for very different $N_{\rm H}^{\rm obs}$ estimated for AS 296 are plotted with dotted lines. Additional depression of the continuum is caused by the iron curtain absorptions (Section 2.2), here denoted by "i.c."

Appendix B
Spectral Energy Distribution during Quiescent and Active Phases of Our Targets

Figure 4 compares the profile of the UV continuum for the investigated objects during the quiescent and active phases (Section 3.1).

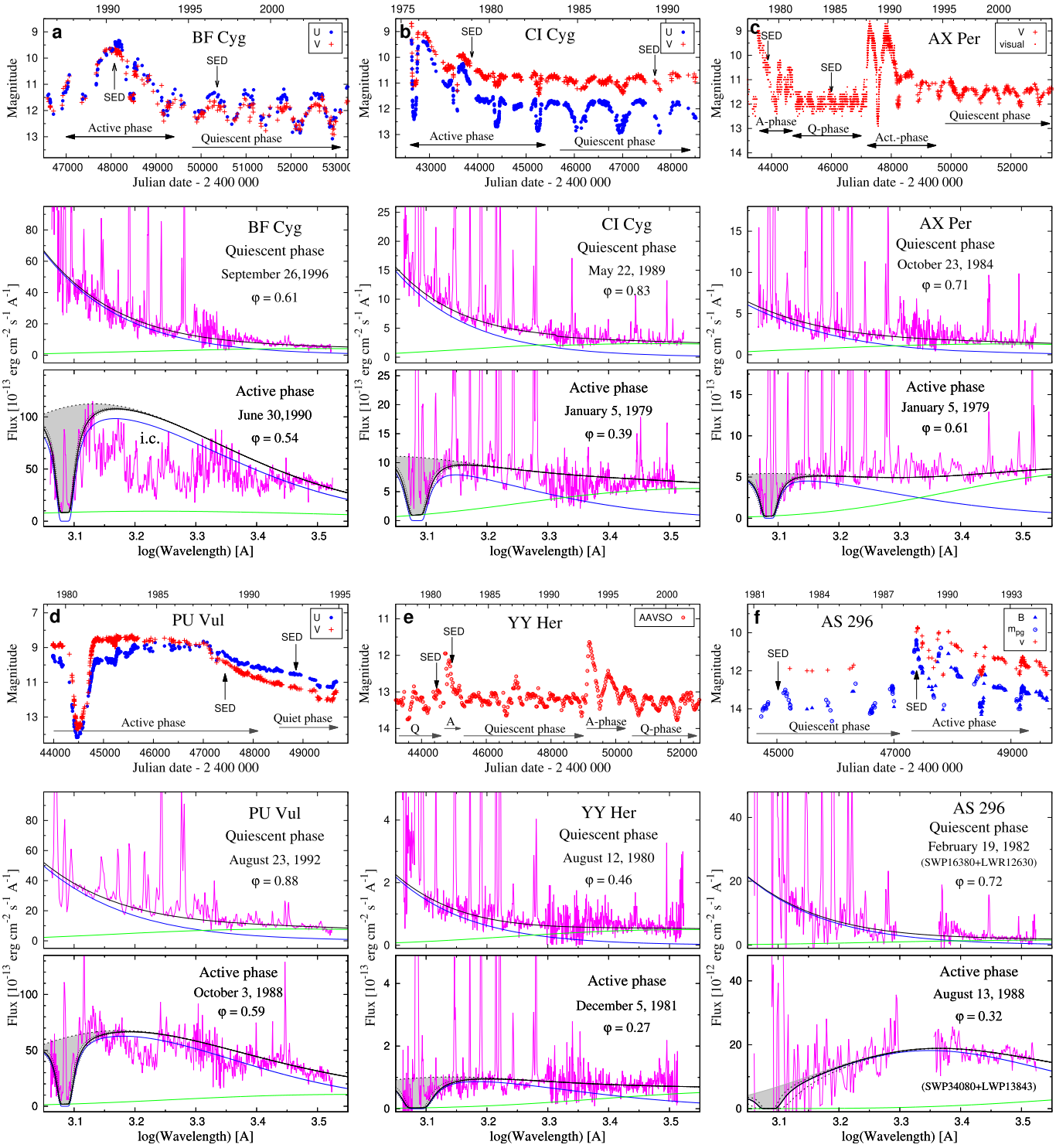

Figure 4. Comparison of SEDs for our targets during quiescent and active phases. Meaning of lines (magenta, black, green, blue, and dotted) and denotation by i.c. are as in Appendix A. Panels for (a) BF Cyg, (b) CI Cyg, (c) AX Per, and (e) YY Her are compiled according to Skopal (2005), and that for PU Vul is adapted from Skopal (2014). In panel (f) we used photometry of Munari et al. (1989, 1992, 1995). The dramatic change of the spectrum during the transition from quiescent to active phase is caused by the creation of a disk-like structure around the WD during outbursts and subsequent formation of the neutral wind region in the orbital plane (Section 3.2). Here the former is evidenced by the emergence of deep eclipses in the light curves (top panels), while the latter is indicated by Rayleigh scattering on atomic hydrogen around the Lyα line (gray area). Note that AR Pav was observed only during the active phase, so its UV spectrum from quiescence is not available. Instead, we show here an example of AS 296, although its far-UV spectrum is not well determined (see Appendix C).

Appendix C
Discussion of the Selection of the Final Set of Targets

In this appendix, we explain why some of the systems suggested in Section 2.1 as candidates cannot be included in the resulting set of our targets. First, we verify whether noneclipsing systems from the second group (i.e., showing the far-UV continuum depression; Z And, TX CVn, and CD −43° 14304) have also a high orbital inclination. Second, we

comment on some eclipsing systems from the first set (i.e., showing the optical eclipses) whose far-UV spectra are underexposed (BX Mon, AS 338, and AS 296), as well as disputed object CH Cyg. The following comments are relevant:

Z And and TX CVn sporadically show eclipses in their optical light curves during active phases, suggesting that their orbital inclination i is quite high (see Skopal et al. 2004). A high i for both systems is also constrained by the two-temperature type of their UV spectrum (see Figures 3 and 6 of Skopal 2005)—a typical spectral feature of symbiotic binaries with a high i that emerges during active phases (Section 1). In addition, an analysis of the 2003 eclipse of Z And suggested $i > 76°$ (Skopal 2003). On the basis of polarimetric observations, Isogai et al. (2010) derived $i = 74° \pm 14°$, and analyzing the Rayleigh scattering effect during quiescence, Skopal & Shagatova (2012) obtained $i = 59°–2°/+3°$, which was later refined to $63\overset{\circ}{.}6 - 12.2/+6\overset{\circ}{.}9$ by Shagatova (2017). A high value of i for Z And is independently supported by the obscuration of the O I] λ1641 emission line around the inferior conjunction of the giant (Shore & Wahlgren 2010; Skopal & Shagatova 2012). As for CD −43°14304, there are no relevant observations to estimate directly its i. Here a relatively high value of i is suggested by the ionization structure during active phases that is constrained for CD −43°14304 by the two-temperature type of the UV spectrum shown by its model SED (see Figure 5 of Skopal 2005). That these three systems have a high i but are not strictly eclipsing explains why the corresponding $N_{\rm H}^{\rm obs}$ values are lower than those measured for eclipsing systems (see Figure 1), as expected according to the ionization structure during active phases.

As for BX Mon, its very faint far-UV continuum does not make it possible to evaluate the effect of Rayleigh scattering. We excluded CH Cyg because its activity is accretion powered and thus does not show typical features of Z And−type outbursts (e.g., Mikolajewska et al. 1988; Tarasova & Skopal 2021). In addition, its basic configuration (binary or triple system) and orbital inclination are uncertain—possible eclipses observed during 1992 and 1994 (Skopal et al. 1996) never repeated again (see Hinkle et al. 2009, for a review). That is probably why the Rayleigh scattering effect was observed only during a short period (from ∼1993 to ∼1995), although CH Cyg is active from ∼1977 (see its light curve[7]). Further, FN Sgr was observed in the UV only during quiescence (e.g., Brandi et al. 2005).

Finally, spectra of AS 338 and AS 296 are strongly underexposed in the far-UV, which precludes a correct determination of $N_{\rm H}^{\rm obs}$ by Rayleigh scattering (see Figure 3, bottom row). This is because the light from both stars is strongly reddened with the color excess $E_{B-V} = 0.5$ (Esipov et al. 2000) and 1.0 (Munari et al. 1992) for AS 338 and AS 296, respectively. Therefore, if we attribute the total attenuation of the far-UV radiation to Rayleigh scattering, we obtain only the upper limits of $N_{\rm H}^{\rm obs}$, or very uncertain values (see Figure 1).

Appendix D
Characteristic Parameters of Targets

In this appendix, we briefly summarize the basic characteristics of the selected targets that are suitable for the aim of this paper—the eclipsing symbiotic binaries with a well-exposed far-UV spectrum acquired during the active phase (see Section 2.1).

Recent ephemerides of the eclipses and/or the inferior conjunction of the red giant, distances, and the E_{B-V} interstellar reddening parameter of the targets are found in Table 1, while Table 2 lists the physical parameters of their main radiation sources. In addition, Table 3 (Appendix E) presents these parameters for the hot component and the nebula we obtained by modeling their UV SEDs in this paper (Section 2.2), while Table 4 of Appendix E collects these parameters for the spectra from quiescent phases, plotted in Figures 2 and 4. Below we briefly describe their photometric observations with regard to the appearance of eclipses in their light curves during active phases.

BF Cyg: In ∼1894 BF Cyg experienced a nova-like explosion (Jacchia 1941), after which its brightness was gradually

Table 2
Characteristic Parameters of the Radiation Sources of Our Targets

Red Giant			Hot Component				Nebula[c]	
Object	ST	$R_{\rm RG}$	$L_{\rm RG}$	$R_{\rm WD}^{\rm eff}$ Q/A	$T_{\rm BB}$ Q/A	$L_{\rm WD}$ Q/A	EM Q/A	Reference
BF Cyg	M 5	150	2700	0.79/7.1	5.5/2.15	5200/16800[a]	3.1/12	1, 2, 3, 11
CI Cyg	M 5.5	180	3400	0.11/0.67	11.5/2.8	1700/1540[a]	0.48/1.1	2, 3, 4
YY Her	M 4	110	1600	<0.14/0.89	>10.5/2.2	>2100/3800[a]	1.1/0.7–1.3	2, 3[e]
AR Pav	M 5	139	2300	–/1.9	–/2.2	–/6400[a]	–/4.6	2, 3, 5, 12
AX Per	M 4.5	102	1200	0.07/0.42	∼10/0.6	400–900/∼1200[a]	0.25/0.30–0.71	2, 3
⋯	M 5.6	115	1500	–/6.2-11	–/0.53–0.63	–/600–1400[a]	–/0.35–0.82[d]	6
PU Vul	M 6-7	282	3820	≈0.03/8.2[b]	≈20/2[b]	≈1000/9700[b]	–/11[b]	7, 8, 9, 10

Notes. Red giant: spectral type ST, radius $R_{\rm RG}$ ($R_\odot$), luminosity $L_{\rm RG}$ ($L_\odot$). Hot component: effective radius $R_{\rm WD}^{\rm eff}$ ($R_\odot$), temperature $T_{\rm BB}$ (10^4 K), luminosity $L_{\rm WD}$ ($L_\odot$), during quiescent (Q) and active (A) phases. Nebula: emission measure EM (10^{60} cm^{-3}).

[a] The luminosity of the 10^5 K hot ionizing source that generates the observed EM during active phases (Skopal et al. 2017).

[b] As on 1988 October 3 (see Table 3).

[c] Symbiotic nebulae radiate at characteristic electron temperature T_e = 13,000–19,000 K during quiescent phases (Muerset et al. 1991; Skopal 2005), while during active phases, an additional high-temperature nebula with $T_e \gtrsim 30{,}000$ K is indicated (see Figures 3, 5, 8, 10, 16, 19, and 21 of Skopal 2005, and Table 3 in Appendix E here).

[d] The out-of-eclipse values.

[e] As on 1981 December 5, for the active phase.

References: (1) Muerset et al. 1991; (2) Mürset & Schmid 1999; (3) Skopal 2005; (4) Skopal et al. 2012; (5) Schild et al. 2001; (6) Skopal et al. 2011; (7) Kato et al. 2012; (8) Shugarov et al. 2012; (9) Chochol et al. 1998; (10) Cúneo et al. 2018; (11) Mikolajewska et al. 1989; (12) Quiroga et al. 2002.

Table 3
Parameters from Model SEDs during Active Phases (Table 1): R_{WD}^{eff}, T_{BB}, T_e, and EM for the Given Date of Observation, and a Minimum of the χ^2_{red} Function

Object	Date yyyy-mm-dd	R_{WD}^{eff} ($R_\odot$)	T_{BB} (K)	T_e (K)	EM (10^{60} cm^{-3})	χ^2_{red} /dof
BF Cyg	1987-08-11	1.7 ± 0.2	25,000 ± 2000	30,000 ± 5000	3.0 ± 0.5	[c]
	1987-11-16	2.0 ± 0.2	25,000 ± 2000	20,000 ± 3000	3.4 ± 0.5	[c]
	1988-03-19	1.1 ± 0.1	45,000 ± 5000	18000 ± 2000	2.6 ± 0.3	1.4/21
	1990-06-30	6.3 ± 0.8	21,500 ± 2000	42000[b] ± 5000	6.9 ± 0.7	[c]
	1990-07-06	6.5 ± 0.6	21,000 ± 2000	30,000[b] ± 5000	8.4 ± 0.8	[c]
	1990-11-05	5.8 ± 0.5	25,000 ± 2000	42000[b] ± 5000	11 ± 1	[c]
CI Cyg	1979-01-05	0.50 ± 0.05	28,000 ± 2000	20,000[a]	0.64 ± 0.07	[c]
	1979-06-11	0.60 ± 0.1	25,000 ± 4000	∼15,000	∼0.37	[d]
	1979-06-29	∼0.54	∼25,000	∼15,000	∼0.40	[d]
	1980-01-30	0.52 ± 0.07	25,000 ± 2000	20,000 ± 2000	0.43 ± 0.06	[c]
	1980-04-14	∼0.44	∼25,000	∼40,000[b]	>0.26	[e]
	1980-08-01	0.44 ± 0.07	25,000 ± 3000	20,000 ± 3000	0.37 ± 0.06	[c]
	1980-08-18	0.49 ± 0.08	25,000 ± 3000	20,000 ± 3000	0.40 ± 0.07	[c]
	1980-08-28	0.46 ± 0.05	28,000 ± 2000	15,000[a]/40,000[b]	0.61 ± 0.05	[c]
	1980-11-14	0.38 ± 0.05	28,000 ± 3000	25,000 ± 3000	0.52 ± 0.07	[c]
	1981-01-08	0.34 ± 0.04	28,000 ± 2000	25,000 ± 3000	0.46 ± 0.05	[c]
	1981-08-14	∼0.36	∼28,000	∼25,000	∼0.46	[d]
	1981-12-11	0.51 ± 0.05	25,000 ± 2000	20,000 ± 2000	0.25 ± 0.04	[c]
YY Her	1981-12-04	1.1 ± 0.2	22,000 ± 2000	15,000 ± 2000	0.66 ± 0.2	1.8/17
AR Pav	1980-10-30	2.7 ± 0.3	16,000 ± 1500	14,000[a]/40,000[b]	3.2 ± 0.4	1.4/14
	1980-11-01	2.7 ± 0.3	16,000 ± 1500	15,500[a]/40,000[b]	3.3 ± 0.4	1.4/15
	1980-11-02	3.1 ± 0.3	16,000 ± 1500	15,500[a]/40,000[b]	3.3 ± 0.4	1.5/17
	1980-11-03	3.0 ± 0.3	16,000 ± 1500	15,500[a]/40,000[b]	4.0 ± 0.5	1.4/17
	1982-07-01	3.5 ± 0.4	16,000 ± 1500	17,000[a]/40,000[b]	4.0 ± 0.5	1.8/17
	1984-03-07	4.4 ± 0.5	16,000 ± 1500	17,000 ± 2000/40,000[b]	3.7 ± 0.5	1.6/12
	1992-07-08	3.9 ± 0.5	16,000 ± 1500	17,000[a]/40,000[b]	2.6 ± 0.3	1.2/11
	1984-04-10	5.5 ± 0.5	15,500 ± 1500	13,500[a]/40,000[b]	4.3 ± 0.5	1.8/13
	1979-07-17	3.5 ± 0.5	19,000 ± 2000	15,800[a]/40,000[b]	3.9 ± 0.4	[c]
	1981-05-10	2.6 ± 0.3	20,000 ± 2000	15,500 ± 2000/40,000[b]	4.0 ± 0.5	0.90/18
	1978-05-16	∼3.6	∼17,000	…	…	[e]
	1978-08-08	2.9 ± 0.5	17500 ± 2000	15,500[a]/40,000[b]	3.5 ± 0.7	2.0/15
	1978-11-11	3.8 ± 0.5	16,000 ± 2000	14,000[a]/40,000[b]	3.3 ± 0.4	[c]
	1980-07-30	4.6 ± 0.7	16,000 ± 2000	15,000[a]/40,000[b]	5.3 ± 0.6	[c]
	1982-04-07	3.2 ± 0.4	16,000 ± 2000	40,000[b]	∼3.2	0.39/127
AX Per	1978-12-31	0.90 ± 0.2	20,000 ± 2000	15,000 ± 2000	0.41 ± 0.06	[c]
	1979-01-05	0.90 ± 0.1	20,000 ± 1000	15,000 ± 2000	0.40 ± 0.05	0.80/18
PU Vul	1988-06-29	6.0 ± 0.7	23,000 ± 2000	15,000 ± 2000	12 ± 2	2.4/18
	1988-07-16	9.8 ± 1.1	19,000 ± 1500	14,000 ± 2000	1.3 ± 0.3	1.5/21
	1988-10-03	8.2 ± 1.0	20,000 ± 2000	20,500 ± 3000	11 ± 2	3.9/212
	1989-04-08	7.2 ± 0.8	22,000 ± 2000	20,000[b]	5.3 ± 1	2.4/16
	1989-05-19	5.5 ± 0.6	24,000 ± 2000	31,000 ± 3000	9.9 ± 2	1.5/15
	1989-09-25	4.2 ± 0.5	27,000 ± 3000	24,000 ± 3000	5.4 ± 0.7	0.88/15
AS 338	1989-10-09	≈2.9	≈15, 000	≈15, 000	≈0.4	[d]
AS 296	1988-08-13	≈8.7	≈13, 000	≈10000	≈0.1	[d]
	1988-11-11	≈4.9	≈15, 000	≈15, 000	≈0.1	[d]
	1990-03-13	≈4.7	≈16, 000	≈20, 000	≈0.1	[d]

Notes.
[a] Fixed value.
[b] High-temperature nebula (T_e fixed) filling in the residual light around Lyα.
[c] From a comparison with a set of synthetic models (Section 2.2).
[d] Underexposed spectrum.
[e] Only SWP spectrum available.

declining for about 70 yr, occasionally showing brightenings lasting for several years (Z And type of outbursts), with maxima of around 1920, 1956, 1968–74, 1990, and 2006 (Leibowitz & Formiggini 2006; Skopal et al. 1997; Munari et al. 2006; Sekeráš et al. 2019). During the 1989–94 active phase, Skopal (1992) reported for the first time the appearance of a primary minimum in the *UBV* light curves (eclipse), which was relatively narrow and rectangular in profile, located around the position of the inferior conjunction of the giant. Later, the eclipsing nature of BF Cyg was also confirmed by observing the effect of Rayleigh scattering near the eclipse during the

[7] e.g., https://www.aavso.org/LCGv2/

Table 4
As in Table 3, but for the Spectra from Quiescent Phases That Are Plotted in Figures 2 and 4

Object	Spectrum	Date (yyyy-mm-dd)	Julian Date (JD 2 44...)	R_{WD}^{eff} ($R_\odot$)	T_{BB} (K)	T_e (K)	EM (10^{60} cm^{-3})	Note
BF Cyg	SWP13477+LWR10132	1981-03-13	44676.84[a]	0.37	100,000[b]	∼5000	∼0.22	[d]
	SWP28734+LWP08681	1986-07-22	46633.58	0.48	100,000[b]	∼22,000	∼3.3	[d]
	SWP58385+LWP32695	1996-09-26	50352.80	0.44	95,000	22,800	2.5	Sk05[c]
CI Cyg	SWP36321+LWP15571	1989-05-22	47669.04	0.088	115,000	24,000	0.31	Sk05
YY Her	SWP09773+LWR08493	1980-08-12	44464.18	<0.14	>105,000	21,500	1.1	Sk05
AX Per	SWP24278+LWP04619	1984-10-23	45997.21	<0.10	>66,000	25,000	0.25	Sk05
PU Vul	SWP45415+LWP23757	1992-08-23	48858.25	<0.64	>79,000	∼25,000	∼9.6	Sk14
AS 296	SWP16380+LWR12630	1982-02-19	45020.11	0.22	100,000[b]	∼20,000	∼0.72	[d]/[e]

Notes.
[a] Orbital phase ∼0.1; $N_H^{obs} \sim 2 \times 10^{23}$ cm^{-2}.
[b] Fixed value.
[c] For the distance $d = 3.4$ kpc (Table 1).
[d] From a comparison with a set of synthetic models (Section 2.2). Sk05—according to Skopal (2005); Sk14—according to Skopal (2014).
[e] Underexposed spectrum.

Table 5
Input Parameters, T_{in}, ρ_{in}, and Resulting Parameters, T_1, ρ_1, $\dot{M}$, R_1, for Modeling the Lyα Profile Formed in the Wind from the WD above Its Pseudophotosphere Using the Code SHELLSPEC

Model No.	T_{in} (K)	ρ_{in} (g cm^{-3})	T_1 (K)	ρ_1 (g cm^{-3})	$\dot{M}$ ($M_\odot$ yr^{-1})	R_1 ($R_\odot$)
1[a]	30,000	1×10^{-10}	24,000	4.4×10^{-11}	1.9×10^{-6}	1.5
2[a]	30,000	4×10^{-10}	17,000	3.9×10^{-11}	7.7×10^{-6}	3.2
3[a]	30,000	2×10^{-9}	14,000	9.5×10^{-11}	3.9×10^{-5}	4.6
4[b]	40,000	9×10^{-11}	25,000	3.5×10^{-11}	1.7×10^{-6}	1.6
5[b]	40,000	1×10^{-10}	21,000	2.8×10^{-11}	1.9×10^{-6}	1.9
6[b]	40,000	1.5×10^{-10}	13,000	1.7×10^{-11}	2.9×10^{-6}	3.0
7[b]	50,000	1×10^{-10}	33,000	4.4×10^{-11}	1.9×10^{-6}	1.5
8[b]	50,000	2×10^{-10}	21,000	3.5×10^{-11}	3.9×10^{-6}	2.4
9[b]	50,000	3×10^{-10}	17,000	3.6×10^{-11}	5.8×10^{-6}	2.9
10[b]	60,000	2×10^{-10}	26,000	3.8×10^{-11}	3.9×10^{-6}	2.3
11[b]	60,000	4×10^{-10}	19,000	3.9×10^{-11}	7.7×10^{-6}	3.2
12[b]	60,000	8×10^{-10}	15,000	5.0×10^{-11}	1.5×10^{-5}	4.0

Notes. Parameters and modeling are described in Appendix F. Corresponding profiles are shown in Figure 5.
[a] Models for temperature gradient, $T(r)/T_{in} = (r/R_{in})^{-1/2}$.
[b] $T(r)/T_{in} = (r/R_{in})^{-1}$.

quiescent phase (Pereira & Landaberry 1996). The following development of the wave-like orbital-related variation during 1995–2005 reflects a quiescent phase of BF Cyg (see Figure 4(a) in Appendix B).

CI Cyg: The eclipsing nature of CI Cyg is best documented by its major active phase that began in 1975 (Belyakina 1976), when narrow minima, eclipses, developed in the light curve during the first four 855.25-day cycles from the maximum, with the subsequent change to a broad wave-like variation since ∼1984 (see Figure 2 of Belyakina & Prokofeva 1991 and Figure 4(b) in Appendix B). This is a textbook example of the typical photometric features of the active and quiescent phases of SySts reflecting the very different ionization structure of the hot component (see Sections 1 and 4.2; Figures 2(c) and 2(f) for a summary).

YY Her: Munari et al. (1997b) identified four Z And−type outbursts with six additional brightenings in the historical (1890–1996) light curve of YY Her. The authors also found four deep and sharp minima in the light curve, located near the zero orbital phase (i.e., at the light minima in their quiescent light curve). However, they rejected their eclipsing nature because they did not find any reason for this interpretation compared to the eclipses observed in SySts. On the other hand, they found no other reasonable explanation for these minima. During the 1993–98 main active phase, the visual light curve of YY Her showed a relatively narrow V-shaped minimum in 1994.43, around the zero orbital phase, suggesting a high orbital inclination, but less than 90° (see, e.g., Figure 16 of Skopal 2005). The eclipsing nature of YY Her was confirmed by measuring the eclipse effect in the *U*-light curve during 1997 (Tatarnikova et al. 2000). The transition to the quiescent phase was similar to that observed for AX Per or CI Cyg (see Figure 1 of Tatarnikova et al. 2001). After entering the quiescent phase, only a few brighter periods have been recorded (Munari et al. 2013, 2021).

AR Pav: The eclipsing nature of AR Pav was already revealed by the first photographic observations made between 1889 and 1936.5 by Mayall & Shapley (1937), who classified it as an unusual eclipsing P Cyg–type binary with an orbital period of 605 days. Later, optical spectroscopy showed that

AR Pav is a symbiotic binary (see Kenyon 1986, and references therein). Observing changes in the eclipse profile and systematic changes in their timing from cycle to cycle, a strong out-of-eclipse variability (e.g., Andrews 1974; Bruch et al. 1994; Skopal et al. 2000; Sekeráš et al. 2019) and also the spectroscopic variability in the UV/optical domain (e.g., Schild et al. 2001; Quiroga et al. 2002) reflect continuous activity of AR Pav. The persistent presence of narrow deep minima—eclipses—in the light curve and current activity indicate that AR Pav is in a long-lasting active phase.

AX Per: The historical light curve of AX Per (since 1887) is characterized by long quiescent phases, occasionally interrupted by Z And−type outbursts of typically several years, usually showing more than one brightening (see, e.g., Figure 1 in Skopal et al. 2011; Figure 1 in Leibowitz & Formiggini 2013). The eclipsing nature of AX Per was unambiguously revealed during the 1988–94 active phase by the appearance of narrow minima around the inferior conjunction of the giant (Skopal & Komárek 1990; Skopal 1991). Figure 4(c) in Appendix B shows this part of the light curve, together with the following development of the quiescent phase since ∼1995. The nature of low stages between outbursts as the quiescent phase of SySts was proven by Kenyon (1982), who revealed the wave-like variation in the light curve between the ∼1950 and ∼1978 outbursts with a period of 681.6 days, which he ascribed to the orbital period.

PU Vul is a symbiotic nova, discovered during its outburst in 1979 by Kozai et al. (1979) and Argyle et al. (1979). From ∼1977 to ∼1979, PU Vul brightened by ∼5 mag in the m_{pg}/B band. Subsequently, from 1980.1 to 1981.4 the light curve of the nova showed a narrow (relative to the orbital period; see below), ∼5 mag deep minimum, after which it continued at a bright stage (a supergiant phase) up to ∼1987.5, when PU Vul began a gradual fading until ∼1999 (the nebular phase). Meanwhile, the light curve showed another relatively narrow but only ∼0.5 mag deep minimum around 1994.25 (see Figure 1 of Tatarnikova et al. 2018, and references therein). Vogel & Nussbaumer (1992) interpreted the first deep minimum as an eclipse of the outbursting star by the M-giant companion. The appearance of the second 1994 eclipse allowed Nussbaumer (1996) to estimate the orbital period of the binary to be 4900 ± 100 days, later refined by Shugarov et al. (2012) to 4897 ± 10 days using three primary minima. Since ∼2000, the development of a broad wave in the light curve with minima around the inferior conjunction of the giant (Tatarnikova et al. 2018)[8] indicates that PU Vul is currently in the quiescent phase.

Appendix E
Physical Parameters of the Ultraviolet Continuum

Table 3 presents other physical parameters of our targets given by the variables of Equation (1) that determines the continuum models for active phases, while Table 4 lists these parameters for the spectra from quiescent phases that are used in Figures 2 and 4. The modeling is introduced in Section 2.2.

[8] See also the current AAVSO light curve: https://www.aavso.org/LCGv2/.

Appendix F
Lyα Line Profiles from Spherically Symmetric Expanding Shell

In this appendix, we test whether the Lyα absorption line profile that can be formed in the expanding wind from the WD during the active phases could be as broad as the attenuation due to Rayleigh scattering on H^0 atoms in the wind from the red giant.

For this purpose, we used the code SHELLSPEC (Budaj & Richards 2004), which solves a simple radiative transfer along the line of sight in the moving circumstellar medium (CSM) assuming local thermodynamic equilibrium (LTE) and single scattering approximations. The LTE model determines the basic CSM structure, temperature, mass density, and electron density as functions of depth.

Here the CSM has the form of spherically symmetric wind from the WD, whose optically thick/thin interface represents the WD's pseudophotosphere (originally suggested for classical nova outbursts by Kato & Hachisu 1994). Synthetic Lyα line profiles are calculated using an object SHELL in the SHELLSPEC code. The radius of the inner (R_{in}) and outer (R_{out}) sphere is set to 1 and 5 $R_\odot$, respectively. We assume that the line profile is formed in the wind from the WD that conforms to wind properties derived from observations during active phases: the mass-loss rate $\dot{M}$ of a few times $10^{-6}\,M_\odot\,\mathrm{yr}^{-1}$ (e.g., Skopal 2006) and the pseudophotosphere expansion velocity of $\approx 200\,\mathrm{km\,s}^{-1}$ (e.g., McKeever et al. 2011) are considered. The latter is given by radial velocities of absorption components in P Cygni profiles of hydrogen Balmer lines measured mainly at the beginning of outbursts. For simplicity, its value was assumed to be constant, and for turbulent motions we adopted a constant velocity of $10\,\mathrm{km\,s}^{-1}$.

Next, we choose the initial temperature and density at the inner radius of the shell, T_{in} and ρ_{in}, deep inside the pseudophotosphere (i.e., where the optical depth in the continuum is $\gg 1$), and find what temperature T_1 and density ρ_1 correspond to the wind medium with an optical thickness of 1, assuming it to represent the WD's pseudophotosphere. Its radius, R_1, is given by the mass continuity equation that determines the densities of the expanding wind. The input parameters T_{in} and ρ_{in} were chosen so that the resulting parameters, T_1, ρ_1, $\dot{M}$, and R_1, were comparable to those determined from observations (Tables 3 and 5).

As the emitted flux at the radial distance r from the WD could basically satisfy the proportionality $\sigma T^4 \propto r^{-2}$, we first provided calculations using the temperature gradient $T(r)/T_{in} = (r/R_{in})^{-1/2}$. For suitable parameters $T_{in} = 30{,}000$–$40{,}000$ K and ρ_{in} = few times 10^{-10} to 10^{-9} $\mathrm{g\,cm}^{-3}$, all the corresponding profiles have a dominant emission component (see Figure 5(a), green profiles), R_1 is of a few solar radii, T_1 is between 14,000 and 24,000 K, and $\dot{M}$ is a few times 10^{-6} to $10^{-5}\,M_\odot\,\mathrm{yr}^{-1}$ (Table 5).

In order to obtain the absorption component in the Lyα profile, we assumed a steeper temperature gradient, $T(r)/T_{in} = (r/R_{in})^{-1}$. The corresponding profiles, calculated for reasonable initial values of T_{in} and ρ_{in}, are shown in Figure 5, where they are compared with the attenuation of the UV continuum around the Lyα line due to Rayleigh scattering on 5×10^{22} and 1×10^{23} hydrogen atoms per cm^2. Despite the fact that we chose rather low values of N_H (see Figure 1), the attenuation effect by Rayleigh scattering is clearly dominant. The specific very broad wings from Rayleigh scattering are

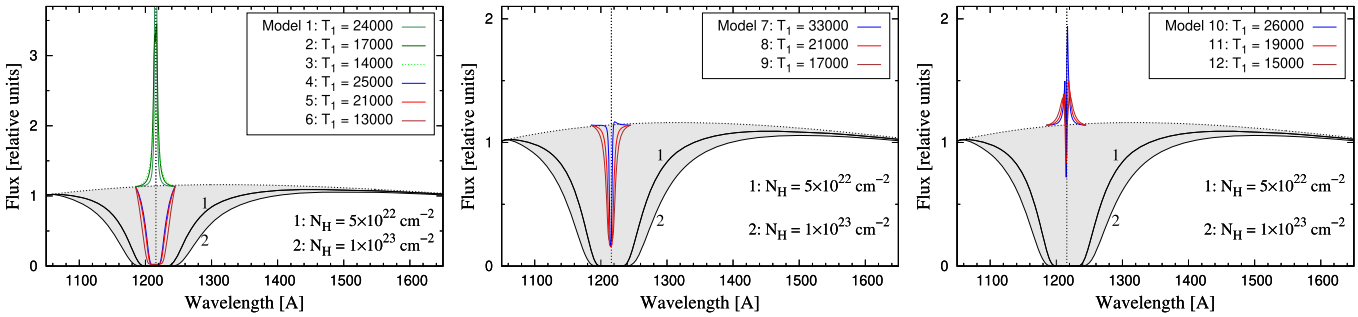

Figure 5. Comparison of the UV continuum attenuation due to Rayleigh scattering on H^0 atoms for two values of N_H (gray area) with the Lyα line profile that may form in the expanding wind from the WD. The modeling of the Lyα line is described in Appendix F. The model parameters are summarized in Table 5. The dotted line represents the unattenuated continuum of the pseudophotosphere with a temperature $T_{BB} = 22{,}000$ K.

significantly broader than the "atmospheric" profile of the Lyα line.[9]

Finally, it is important to note that if the width of the "atmospheric" Lyα absorption profile were dominant, it would not be possible to measure the orbital phase dependence of N_H^{obs}. Instead, the N_H^{obs} values would be scattered along the orbital phase, as they would be dependent on the properties of the WD's pseudophotosphere, i.e., on the object and its current activity. This is not observed. In our case, the optically thick pseudophotosphere plays only the role of blocking ionization photons from the central WD, which has nothing to do with its properties.

Appendix G
On the Effect of Interstellar Extinction on Modeling the UV Continuum

The strong attenuation of radiation by interstellar dust particles around the wavelength of 2175 Å is often used to determine the characteristic interstellar absorption from the UV spectrum. Since the profile of the true continuum can be determined with an accuracy of about 10%, this uncertainty also limits the value of the color excess, so that the corrected profile of the continuum around 2175 Å does not show a local extreme.

Figure 6 shows what the effect of interstellar reddening looks like in the range of IUE spectra. It plots the Planck function for $T_{BB} = 22{,}000$ K, attenuated by Rayleigh scattering on 5×10^{22} (panel (a) and 1×10^{24} (panel (b)) hydrogen atoms, both dereddened with $E_{B-V} \pm 0.05$ mag, where E_{B-V} is the correct value of the color excess. The value of N_H^{obs} is given by the width of the absorption core and the extension of its wings due to Rayleigh scattering (Section 2.2). Since the extinction curve is wavelength dependent, increasing toward shorter wavelengths, one can expect that N_H^{obs} values determined from the (broad) continuum depression around the Lyα line can be affected also by the uncertainty in E_{B-V}. Moreover, the determination of lower values of N_H^{obs} that attenuate a narrower range of the spectrum will probably be less affected by a change in color excess than high N_H^{obs} values that attenuate a wider range of the spectrum.

Therefore, in order to test how the uncertainties of the color excess affect the determination of N_H^{obs}, we selected one spectrum with a narrow absorption and another one with very broad absorption, which are typical for the superior and inferior conjunction of the red giant, respectively. Specifically, we modeled the spectrum of PU Vul exposed on 1988 October 3 ($\varphi = 0.59$, $N_H^{obs} = 3.9 \times 10^{22}$ cm^{-2}) and the spectrum of AR Pav taken on 1982 April 7 ($\varphi = 0.92$, $N_H^{obs} = 1.0 \times 10^{24}$ cm^{-2}) dereddened with different values of E_{B-V}. For PU Vul we used $E_{B-V} = 0.30 \pm 0.04$, although Kato et al. (2012) give an uncertainty of only ± 0.02, and for AR Pav we adopted $E_{B-V} = 0.26 \pm 0.03$ according to models of Kenyon & Webbink (1984). The corresponding SED models are shown in Figure 7, and their parameters are introduced in Table 6.

In the case of PU Vul (a narrower absorption), N_H^{obs} decreases with increasing E_{B-V} for acceptable χ^2_{red} (Table 6). This is because dereddening the spectrum with a larger value of E_{B-V} will increase the height of the absorption core relative to its long-wavelength wing, leading to a narrowing of the absorption core and thus a decrease of the corresponding N_H^{obs}. According to our models of PU Vul, E_{B-V} uncertainties of ~13% correspond to errors in N_H^{obs} of less than 10% (see Table 6).

In the case of AR Pav, the SED modeling revealed the opposite behavior. This is due to the fact that a strong component of the hot nebular continuum contributes to the far-UV, which shifts the absorption core well above the zero value (see Figure 7, right). As a result, dereddening the spectrum with a higher value of E_{B-V} will increase the level of the far-UV spectrum more than its mid-UV part, which leads to relative smoothing of the absorption core that corresponds to a higher value of N_H^{obs}. Here the uncertainties in E_{B-V} of ± 0.03 mag (~12%) cause errors in N_H^{obs} of 10%–20%. However, the uncertainly of 20%, corresponding to the model for $E_{B-V} = 0.029$, is overestimated because of the worse model —the flux points near 2175 Å are above the model, which increases the value of χ^2_{red} (see Figure 7 and Table 6). Finally, we also tested a model with $E_{B-V} = 0.35$ that can be found in the literature (i.e., the uncertainty of ~35%). However, the points near 2175 Å were ~25% above the model, and χ^2_{red} increased by a factor of ~2 (Table 6).

According to these examples, we assume that interstellar reddening uncertainties may cause additional errors in the N_H^{obs} determination of about 10%.

[9] Note that the gas pressure at the expanding pseudophotosphere is zero, so the broadening of spectral lines by the Stark effect does not apply.

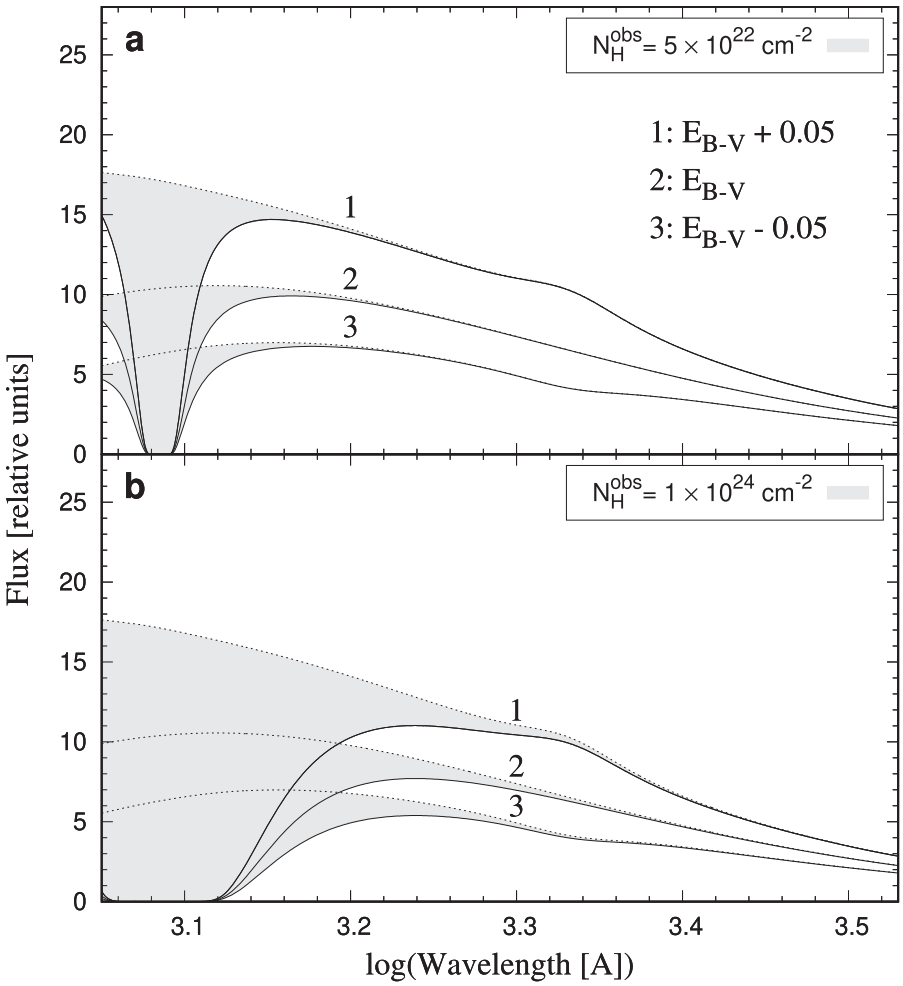

Figure 6. Effect of interstellar extinction in the range of IUE spectra shown for the Planck function ($T_{BB} = 22{,}000$ K) attenuated with (a) $N_H^{obs} = 5 \times 10^{22}$ and (b) 1×10^{24} cm^{-2} and dereddened with $E_{B-V} \pm 0.05$ mag (see text). Meaning of lines and the gray area is as in Figure 3.

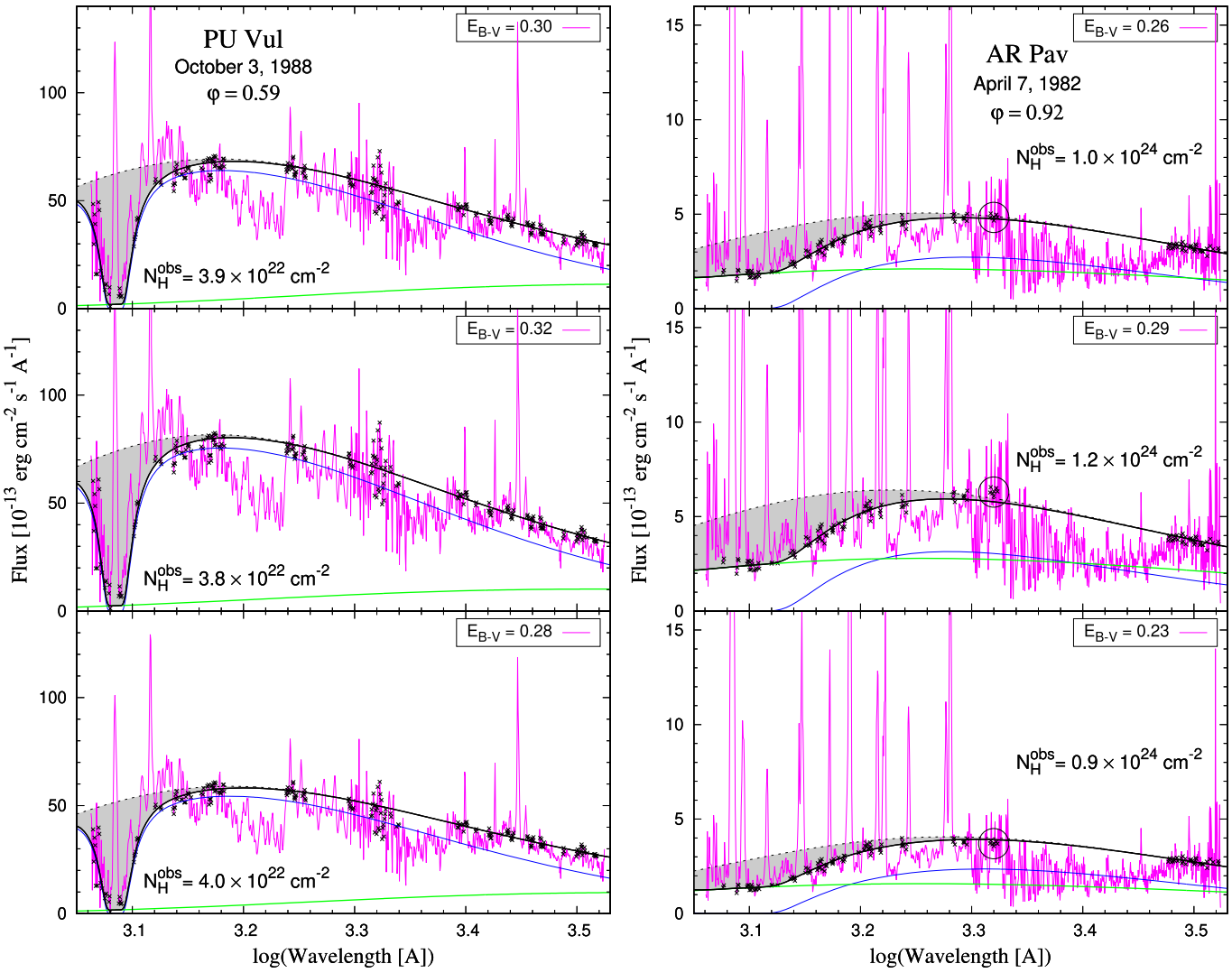

Figure 7. A possible effect of interstellar extinction on the determination of $N_{\rm H}^{\rm obs}$ illustrated for PU Vul (left) and AR Pav (right). The former and the latter represent the cases with relatively small and high values of $N_{\rm H}^{\rm obs}$ measured around the superior and the inferior conjunction of the red giant, respectively. The crosses represent the flux points that we modeled. The large spread of selected points near 2175 Å for PU Vul is responsible for the high $\chi^2_{\rm red}$ value, while the small spread of these points for AR Pav (circled) demonstrates the sensitivity of the spectrum in this region to interstellar extinction. Meaning of lines and the gray area is as in Figure 3. Corresponding parameters are summarized in Table 6.

Table 6
The Best-fit Parameters Corresponding to SED Models of PU Vul and AR Pav Plotted in Figure 7

Object	E_{B-V} (mag)	$N_{\rm H}^{\rm obs}$ (cm^{-2})	$R_{\rm WD}^{\rm eff}$ ($R_\odot$)	$T_{\rm BB}$ (K)	T_e (K)	EM (10^{60} cm^{-3})	$\chi^2_{\rm red}$ /dof
PU Vul	0.26	4.2×10^{22}	7.5	19,500	19,000	9.3	4.4/212
	0.28	4.0×10^{22}	8.1	19,500	20,000	9.7	4.1/212
	0.30	3.9×10^{22}	8.2	20,000	20,000	11	3.9/212
	0.32	3.8×10^{22}	9.0	20,000	22,000	11	3.8/212
	0.34	3.5×10^{22}	9.8	20,000	22,000	12	3.8/212
AR Pav	0.23	0.9×10^{24}	3.5	15,000	40,000[a]	2.4	0.40/127
	0.26	1.0×10^{24}	3.2	16,000	40,000[a]	3.2	0.39/127
	0.29	1.2×10^{24}	2.8	17500	40,000[a]	4.2	0.46/127
	0.35	1.2×10^{24}	2.7	19,000	40,000[a]	7.0	0.99/127

Notes. Models are calculated for different values of the color excess E_{B-V}. Denotation and meaning are as in Tables 1 and 3.
[a] Fixed value.

ORCID iDs

Augustin Skopal https://orcid.org/0000-0002-8312-3326

References

Andrews, P. J. 1974, MNRAS, 167, 635
Argyle, R. W., Liller, W., Schwartz, G., et al. 1979, IAU Circ., 3348, 2
Belczyński, K., Mikołajewska, J., Munari, U., Ivison, R. J., & Friedjung, M. 2000, A&AS, 146, 407
Belyakina, T. S. 1976, IBVS, 1169, 1
Belyakina, T. S. 1992, IzKry, 84, 49
Bermúdez-Bustamante, L. C., García-Segura, G., Steffen, W., & Sabin, L. 2020, MNRAS, 493, 2606
Blondin, J. M., Kallman, T. R., Fryxell, B. A., & Taam, R. E. 1990, ApJ, 356, 591
Blondin, J. M., Stevens, I. R., & Kallman, T. R. 1991, ApJ, 371, 684
Boyarchuk, A. A., Esipov, V. F., & Moroz, V. I. 1966, SvA, 10, 331
Brandi, E., Mikołajewska, J., Quiroga, C., et al. 2005, A&A, 440, 239
Bruch, A., Niehues, M., & Jones, A. F. 1994, A&A, 287, 829
Budaj, J., & Richards, M. T. 2004, CoSka, 34, 167
Cariková, Z., & Skopal, A. 2012, A&A, 548, A21
Chomiuk, L., Linford, J. D., Yang, J., et al. 2014, Natur, 514, 339
Crowley, C., Espey, B. R., & McCandliss, S. R. 2005, in ESA Special Publication 560, 13th Cambridge Workshop on Cool Stars, Stellar Systems and the Sun, ed. F. Favata et al. (Paris: ESA), 343
Dmitrienko, E. S. 2000, AstL, 26, 520
Dumm, T., Schmutz, W., Schild, H., & Nussbaumer, H. 1999, A&A, 349, 169
El Mellah, I., Bolte, J., Decin, L., Homan, W., & Keppens, R. 2020, A&A, 637, A91
Esipov, V. F., Kolotilov, E. A., Mikolajewska, J., et al. 2000, AstL, 26, 162
Fekel, F. C., Hinkle, K. H., Joyce, R. R., & Skrutskie, M. F. 2001, AJ, 121, 2219
Fernandez-Castro, T., Gonzalez-Riestra, R., Cassatella, A., Taylor, A. R., & Seaquist, E. R. 1995, ApJ, 442, 366
González-Riestra, R., Viotti, R. F., Iijima, T., et al. 2008, A&A, 481, 725
Gromadzki, M., Mikołajewska, J., & Soszyński, I. 2013, AcA, 63, 405
Hinkle, K. H., Fekel, F. C., Joyce, R. R., & Wood, P. 2013, ApJ, 770, 28
Horne, K., Marsh, T. R., Cheng, F. H., Hubeny, I., & Lanz, T. 1994, ApJ, 426, 294
Ikonnikova, N. P., Burlak, M. A., Arkhipova, V. P., & Esipov, V. F. 2019, AstL, 45, 217
Isliker, H., Nussbaumer, H., & Vogel, M. 1989, A&A, 219, 271
Jacchia, L. 1941, BHarO, 915, 17
Kato, M., & Hachisu, I. 1994, ApJ, 437, 802
Kato, M., Mikołajewska, J., & Hachisu, I. 2012, ApJ, 750, 5
Kenyon, S. J. 1982, PASP, 94, 165
Kenyon, S. J. 1986, The Symbiotic Stars (Cambridge: Cambridge Univ. Press)
Kenyon, S. J., Fernandez-Castro, T., & Stencel, R. E. 1988, AJ, 95, 1817
Kenyon, S. J., & Webbink, R. F. 1984, ApJ, 279, 252
Kozai, Y., Kuwano, Y., Mattei, J., & Annal, R. 1979, IAU Circ., 3344, 1
Kretschmar, P., El Mellah, I., Martínez-Núñez, S., et al. 2021, A&A, 652, A95
Lee, Y.-M., Kim, H., & Lee, H.-W. 2022, ApJ, 931, 142
Leedjärv, L., Gális, R., Hric, L., Merc, J., & Burmeister, M. 2016, MNRAS, 456, 2558
Leibowitz, E. M., & Formiggini, L. 2008, MNRAS, 385, 445
Leibowitz, E. M., & Formiggini, L. 2013, AJ, 146, 117
Leibowitz, E. M., & Formiggini, L. 2006, MNRAS, 366, 675
Li, K.-L., Metzger, B. D., Chomiuk, L., et al. 2017, NatAs, 1, 697
Manousakis, A., Walter, R., & Blondin, J. M. 2012, A&A, 547, A20
Matthews, L. D., & Karovska, M. 2006, ApJL, 637, L49
McKeever, J., Lutz, J., Wallerstein, G., Munari, U., & Siviero, A. 2011, PASP, 123, 1062
Mikolajewska, J., & Kenyon, S. J. 1992, AJ, 103, 579
Mikolajewska, J., & Kenyon, S. J. 1996, AJ, 112, 1659
Mikolajewska, J., Selvelli, P. L., & Hack, M. 1988, A&A, 198, 150
Muerset, U., Nussbaumer, H., Schmid, H. M., & Vogel, M. 1991, A&A, 248, 458
Munari, U., Buson, L. M., & Massone, G. 1989, A&A, 214, L5
Munari, U., Dallaporta, S., Castellani, F., et al. 2013, ATel1, 4996, 1
Munari, U., Kolotilov, E. A., Popova, A. A., & Yudin, B. F. 1997a, ARep, 41, 802
Munari, U., Rejkuba, M., Hazen, M., et al. 1997b, A&A, 323, 113
Munari, U., Siviero, A., Moretti, S., et al. 2006, CBET, 596, 1
Munari, U., Whitelock, P. A., Gilmore, A. C., et al. 1992, AJ, 104, 262
Munari, U., Yudin, B. F., Kolotilov, E. A., & Gilmore, A. C. 1995, AJ, 109, 1740
Mürset, U., & Schmid, H. M. 1999, A&AS, 137, 473
Nussbaumer, H. 1996, A&A, 307, 470
Nussbaumer, H., Schmid, H. M., & Vogel, M. 1989, A&A, 211, L27
Nussbaumer, H., & Vogel, M. 1987, A&A, 182, 51
Pereira, C. B., & Landaberry, S. J. C. 1996, AJ, 111, 1329
Quiroga, C., Mikołajewska, J., Brandi, E., Ferrer, O., & García, L. 2002, A&A, 387, 139
Rahin, R., & Behar, E. 2023, arXiv:2302.10953
Schild, H., Dumm, T., Mürset, U., et al. 2001, A&A, 366, 972
Schmid, H. M., & Schild, H. 2002, A&A, 395, 117
Seal, P. 1990, Ap&SS, 174, 321
Seaquist, E. R., Krogulec, M., & Taylor, A. R. 1993, ApJ, 410, 260
Seaquist, E. R., Taylor, A. R., & Button, S. 1984, ApJ, 284, 202
Sekeráš, M., Skopal, A., Shugarov, S., et al. 2019, CoSka, 49, 19
Shagatova, N. 2017, PASP, 129, 067001
Shagatova, N., & Skopal, A. 2017, A&A, 602, A71
Shagatova, N., Skopal, A., & Cariková, Z. 2016, A&A, 588, A83
Shagatova, N., Skopal, A., Shugarov, S. Y., et al. 2021, A&A, 646, A116
Shore, S. N., & Aufdenberg, J. P. 1993, ApJ, 416, 355
Shugarov, S., Chochol, D., & Kolotilov, E. 2012, BaltA, 21, 150
Siviero, A., Munari, U., Moretti, S., et al. 2007, BaltA, 16, 55
Skopal, A. 1992, IBVS, 3780, 1
Skopal, A. 1998, A&A, 338, 599
Skopal, A. 2005, A&A, 440, 995
Skopal, A. 2006, A&A, 457, 1003
Skopal, A. 2008, JAVSO, 36, 9
Skopal, A. 2019, ApJ, 878, 28
Skopal, A. 2023, Zenodo, doi:10.5281/zenodo.7695015
Skopal, A., Bode, M. F., Lloyd, H. M., & Tamura, S. 1996, A&A, 308, L9
Skopal, A., Djurašević, G., Jones, A., et al. 2000, MNRAS, 311, 225
Skopal, A., & Komárek, Z. 1990, CoSka, 20, 99
Skopal, A., Pribulla, T., Vaňko, M., et al. 2004, CoSka, 34, 45
Skopal, A., & Shagatova, N. 2012, A&A, 547, A45
Skopal, A., Shugarov, S., Vaňko, M., et al. 2012, AN, 333, 242
Skopal, A., Shugarov, S. Y., Munari, U., et al. 2020, A&A, 636, A77
Skopal, A., Shugarov, S. Y., Sekeráš, S. Y., et al. 2017, A&A, 604, A48
Skopal, A., Tarasova, T. N., Cariková, Z., et al. 2011, A&A, 536, A27
Skopal, A., Teodorani, M., Errico, L., et al. 2001, A&A, 367, 199
Skopal, A., Vittone, A., Errico, L., et al. 1997, MNRAS, 292, 703
Skopal, A., Vittone, A. A., Errico, L., et al. 2006, A&A, 453, 279
Tarasova, T. N., & Skopal, A. 2021, AstL, 47, 235
Tatarnikova, A., Burlak, M., Kolotilov, E., et al. 2018, RAA, 18, 098
Tatarnikova, A. A., Esipov, V. F., Kolotilov, E. A., et al. 2001, AstL, 27, 703
Tatarnikova, A. A., Rejkuba, M., Buson, L. M., et al. 2000, ARep, 44, 190
Tomov, T. V., Stoyanov, K. A., & Zamanov, R. K. 2016, MNRAS, 462, 4435
Vogel, M. 1991, A&A, 249, 173
Vogel, M., & Nussbaumer, H. 1992, A&A, 259, 525
Webster, B. L., & Allen, D. A. 1975, MNRAS, 171, 171
Wiese, W. L., Smith, M. W., & Glennon, B. M. 1966, Atomic transition probabilities. Vol. I: Hydrogen through Neon. A critical data compilation (Washington D.C: U.S. Government Printing Office)